X-RAY THERMAL DIFFUSE SCATTERING AND ITS STUDIES OF LATTICE DYNAMICS

BY

RUQING XU

DISSERTATION

Submitted in partial fulfillment of the requirements
For the degree of Doctor of Philosophy in Physics
in the Graduate College of the
University of Illinois at Urbana-Champaign, 2010

Urbana, Illinois

Doctoral Committee:

Associate Professor Peter Abbamonte, Chair
Professor Tai-Chang Chiang, Director of Research
Professor Paul Goldbart
Professor Naomi Makins

Abstract

X-ray scattering by lattice thermal vibrations give rise to thermal diffuse scattering (TDS). TDS contain valuable information about lattice dynamics of the scattering material. Historically, x-ray TDS was the first tool utilized by people in experimental determination of phonon dispersion relations. With the advent of synchrotron radiation technology, it has reemerged as an efficient probe for phonon studies in the recent decade.

The scattering can be described with a semi-classical theory, and is often decomposed into first-order and high-order processes. First-order TDS, with a simple theoretical formula, is usually the dominating component and often used as an approximation to the total intensity. However, rigorous evaluation of high-order scattering has never been truly performed in the past, due largely to the apparent mathematical complexity of its expression. An algorithm aimed at resolving this difficulty is developed by the author, and proves to be successful.

As a tool of phonon study, TDS was applied to the system of gallium-stabilized δ-plutonium. This material shows curious features in its phonon dispersion relation at room temperature; one of them was conjectured to exhibit further changes when temperature is lowered towards a structural phase transition at ~ 170 K. A TDS experiment was carried out to verify this prediction, yet analysis of the data showed that it was incorrect.

In another major project, a new experimental approach was proposed to allow extraction of phonon dispersion information from measured TDS data without relying on any presumed force-constant models, which were required in previous TDS works and pose a limit to the method's accuracy. The new approach determines frequencies of specific phonon modes based on the temperature-dependence of TDS intensities. A benchmark test of the approach on copper yielded excellent agreement with known phonon dispersion data.

To My Parents

Acknowledgements

Completion of the thesis works described herein would be impossible without the guidance of my advisor, Professor T.-C. Chiang, with whom I have learned an invaluable amount in terms of both scientific knowledge and wisdom of life. Thoughtful discussions with him throughout my Ph.D. years have always been inspiring in generating new research ideas or creating a deeper understanding in physical problems. Many thanks are also owed to Dr. Hawoong Hong at the Argonne National Lab, who has trained me to become a qualified x-ray experimentalist from almost absolute zero. I am also very grateful to Dr. Joe Wong, who is now retired, at the Lawrence Livermore National Laboratory; with him there was a great collaborative experience in the project of plutonium phonons.

I have received numerous helps and supports from the past and current members of the Chiang National Lab, including Peter Czoschke, Leo Basile, Dom Ricci, Mary Upton, Shu-Jung Tang, Juno Lee, Nathan Speer, Aaron Gray, Jaseung Ku, Yang Liu, Matt Brinkley, Longxiang “James” “*xiaopang*” Zhang, and Guang Bian. Thanks also go to the knowledgeable and helpful staffs at Sector 33 of the Advanced Photon Source: Paul Zschack, Zhan Zhang, and Jenia Karapetrova.

More could be said on a personal level, as adapting to lives at somewhere on the other hemisphere of this planet has been a remarkable experience, and it would have been difficult without the supports from my family and my friends. This page would become extremely long if the individual persons and causes were listed one by one. – It is fortunate for me to have them in my life and I will remember them all by my heart.

Table of Contents

Chapter 1 Introduction 1
1.1 Overview: phonon measurement and x-ray TDS 1
1.2 A historical review 2
List of references 5
Chapter 2 Theory 7
2.1 X-ray scattering by matter 7
2.2 Phonons 23
2.3 Classical theory of x-ray TDS 28
List of references 35
Chapter 3 Numerical Simulation 37
3.1 Evaluation of high-order TDS 37
3.2 Examples and discussion 47
List of references 53
Chapter 4 TDS as a Method of Phonon Study 54
4.1 X-ray instruments 54
4.2 Probing phonons with TDS 57
List of references 61
Chapter 5 Phonons in Plutonium 62
5.1 Introduction 62
5.2 Experiment 65
5.3 Data and analysis 67
5.4 Discussion 69
List of references 72
Chapter 6 Momentum-Resolved X-Ray Calorimetry 73
6.1 Motivation 73
6.2 Theory 74
6.3 Example of Cu 75
List of references 80
Chapter 7 Summary and Outlook 81
Author's Biography 83

1 Introduction

1.1 Overview: phonon measurement and x-ray TDS

Phonons are elementary quanta of the thermal vibrations of atomic lattices in crystals. The energy-momentum relationship of normal-mode lattice waves, i.e., the phonon dispersion relation, represents one of the fundamental physical properties of a crystalline material. At present, two major techniques for the experimental measurement of phonon dispersion relations are inelastic neutron scattering (INS) and inelastic x-ray scattering (IXS). In both methods, samples of crystalline materials are investigated with a beam of probe particles (neutrons or x-ray photons); by making measurements on the scattered particles at selected scattering angles, the energy and momentum of particular phonon modes can be directly determined. Developed since the 1950s, INS has been widely applied in numerous solid systems as a standard technique of phonon measurement. IXS with energy-resolution capable of phonon detection was developed in more recent years, yet it has since seen a rapid growth in interest and has found its application in many condensed-matter systems.

Although both methods have been largely successful, certain limitations do exist in their respective applications. For instance, INS is not suitable for materials with high neutron absorption cross sections, and usually requires a large sample size as neutron beams are difficult to focus. IXS is free from these issues, yet its instrumentation is rather complicated and expensive. Third-generation synchrotron beamlines for high energy-resolution IXS (ΔE ~ a few meV or less), which are typically required by phonon studies, are only available at a small number of facilities in the world at present time. Also the data acquisition rate of IXS is not high, as incident photon flux is usually

sacrificed in achieving higher energy resolution; typical data collection takes hours for a single point, and may take up to weeks for a complete mapping of phonon dispersion curves in the reciprocal space.

On the other hand, x-ray thermal diffuse scattering (TDS) has recently emerged as another viable probe of lattice dynamics. – Diffuse scattering of x-ray occurs when a monochromatic x-ray beam is scattered by a crystal with an imperfect lattice. Such imperfections could be due to a variety of reasons, such as stress, impurities, defects, grain boundaries, and so on. Among them the most universal factor is the thermal vibration of the crystal lattice, and the corresponding diffuse scattering is termed *thermal diffuse scattering*, or *temperature diffuse scattering*, both abbreviates to TDS. Although TDS is often considered an undesirable background in x-ray crystallography, its direct connection with lattice dynamics makes it a good probe of the phonon dispersion relations. Advantages of TDS measurements include simple experimental setup, fast data acquisition rate, and the applicability to small or polycrystalline samples, making it a technique much complementary to the existing methods of INS and IXS. – In this dissertation we will present a detailed review on the development, theory, and applications of x-ray TDS.

1.2 A historical review

Shortly before Laue's milestone experiment of x-ray crystallographic diffraction in 1912, concerns were raised to him by Sommerfeld et al. that the intrinsic thermal motion of atoms might impair the predicted diffraction pattern and prevent it from being observed [1]. This was probably the earliest consideration of thermal effects on x-ray diffractions. However, it was based on the very limited knowledge on the microscopic structure of crystals at the time, and was soon proved wrong by Laue's work. – The first systematic theory on this problem was presented one year later, in 1913, by Debye. Based on classical statistics and Einstein's theory of specific heats, Debye concluded that a

thermally vibrating crystal lattice should give rise to attenuated Bragg peaks and a general diffuse background [2,3]. Although the conclusion was qualitatively correct, Debye's theory was incomplete and contained errors [3]. In the next a few years, with the advent in theory of lattice dynamics by Born and von Kármán [4], notable contributions were made to the subject matter by Debye [5], Schrödinger [6], Brillouin [7], Faxén [8] and Waller [9]. The first complete derivation of the TDS formula, with the most general types of crystals considered, was given by Waller in 1925 [10]. Theories at this point have been semi-classical only, namely, amplitudes of vibration modes were computed according to quantum statistics while motions of individual atoms were treated in the framework of classical mechanics; the results, nonetheless, were later confirmed to be correct through rigorous quantum-mechanical derivations by Waller [11] and Ott [12].

Experimentally, it was discovered as early as in 1913 that well-exposed x-ray Laue images of KCl shows unexpected streaks that are not part of the Laue diffraction pattern [13]; similar "extra reflexions" were also found with many other substances in the following years. Among the various explanations proposed [14], Faxén [8] was the first to suggest a connection of the phenomenon to the thermal vibrations of the crystal lattice. Faxén's theory, later generalized by Waller [10] and known as the Faxén-Waller theory, was eventually proved correct by a comprehensive study by Laval in 1938 and 1939 [15] and a number of experiments by others. – For more comprehensive reviews on the early theoretical and experimental developments of x-ray TDS, readers are referred to the reports by Born in 1942 [3], and by Longsdale in 1942 [14] and 1943 [16]. – On a side note, the terms "diffuse scattering" and "temperature diffuse scattering" were probably first coined by Zachariasen [16,17].

The possibility of utilizing TDS as a probe of phonon dispersions was proposed in Longsdale's 1942 paper [14]. However it was not until 1948 that the idea was first realized by Olmer in a study of single crystal aluminum [18]. Following this pioneering work, lattice dynamics of a number of systems were examined by x-ray TDS in the next

decade, including α-Fe by Curien [19], β-brass by Cole and Warren [20], AgCl by Cole [21], Zn by Joynson [22], Cu by Jacobsen [23] and Al by Walker [24].

Early applications of the TDS method were limited, however, by its low accuracy and efficiency. As the cross section of TDS is rather small, the limited brightness of the x-ray tube sources affects not only the data acquisition rate, but also the signal-noise ratio and the angular resolutions in reciprocal space. The limited computational power at the time may also lead to insufficient accuracy in the force-constant analysis. In the mean time, the 1950s also saw the invention and rapid development of neutron scattering as a more convenient and accurate method of phonon study, and the TDS method was soon largely overshadowed. Nonetheless, a few studies were carried out in the following years, including the work on KCl by Boccara [25], NaCl by Buyers and Smith [26], V by Colella and Batterman [27], InAs by Orlova [28], and VSi by Sirota and Orlova [29].

It was not until the recent decade that interest in TDS has revived, much due to the advent in the synchrotron x-ray sources and the related instrumentations. Third-generation synchrotron sources nowadays may generate well-collimated x-ray beams with brightness many orders of magnitude higher than the conventional x-ray tubes. Two-dimensional x-ray detectors, such as image plates, allow parallel measurements with excellent quantum efficiency over a large solid angle. Such capabilities make it possible to carry out highly efficient and precise TDS measurements. Meanwhile modern computational capabilities have enabled efficient quantitative analysis of experimental data with sophisticated modeling. In 1999, Wu *et al.* [30] studied TDS patterns from silicon single crystals using monochromatic x-rays generated from a third-generation synchrotron source. The main features in the experimental TDS patterns were well explained by silicon's phonon dispersion relations. Similar patterns of TDS were also observed by Hastings [31] at about the same time. Later in the same year, Holt *et al.* [32,33] successfully determined phonon dispersion relations of silicon from the experimental TDS images, using a lattice dynamics model that included force constants up to the sixth nearest neighbors. Similar approach was

later applied in the studies of niobium [34] and δ-plutonium [35]. In 2001, Holt *et al.* further applied TDS to map the detailed behavior of a soft zone-boundary phonon mode associated with a charge-density-wave transition in $TiSe_2$ [36], which has been difficult for neutron scattering due to interference from an intense central peak. The method was also used in a study of the antiferrodistortive phase transition in $SiTiO_3$ [37] in 2007.

Chapter 2 of this dissertation will focus on the theoretical background of TDS, starting from the fundamental discussions on x-ray scattering by free and bound-state electrons. Issues concerning numerical simulation of TDS intensities will be examined in Chapter 3, with an emphasis on the evaluation of high-order scattering. Chapter 4 will review basic experimental aspects of TDS measurements, and the chapter next to it will present our experimental work investigating the lattice dynamics in δ-plutonium in relation to one of its structural phase transitions. Finally, a recent development of the TDS method, the momentum-resolved x-ray calorimetry, will be discussed in Chapter 6 before the summary and outlook.

List of References

[1] P. P. Ewald (editor), and numerous crystallographers. *Fifty Years of X-ray Diffraction* (Published for the International Union of Crystallography by N.V.A. Oosthoek's Uitgeversmaatschappij, Utrecht, the Netherlands, 1962).
[2] P. Debye, *Verh. Dtsch. Phys. Ges.* **15**, 678, 738 (1913) 857.
[3] M. Born, *Rep. Prog. Phys.* **9** (1943) 294.
[4] M. Born and T. von Kármán, *Phys. Z.* **13** (1912) 297; *Phys. Z.* **14** (1913) 15; *Phys. Z.* **14** (1913) 65.
[5] P. Debye, *Ann. Phys.* **348** (ser. 4, vol. 43, 1914) 49.
[6] E. Schrödinger, *Phys. Z.* **15** (1914) 79; *ibid*., **15** (1914) 497.
[7] L. Brillouin, *Ann. Phys. Paris* **17** (1922) 88.
[8] H. Faxén, *Z. Phys.* **17** (1923) 266.
[9] I. Waller, *Z. Phys.* **17** (1923) 398.
[10] I. Waller (PhD diss., Uppsala University, 1925).

[11] I. Waller, *Z. Phys.* **51** (1928) 213.
[12] H. Ott, *Ann. Phys.* **416** (ser. 5, vol. 23, 1935) 169.
[13] W. Friedrich, *Phys. Z.* **14** (1913) 1082.
[14] K. Longsdale, *Proc. Phys. Soc.* **54** (1942) 314
[15] J. Laval, *C. R. Acad. Sci.* **207** (1938) 169; *ibid*., **208** (1939) 1512; *Bull. Soc. Franç. Minér.* **64** (1941) 1.
[16] K. Longsdale, *Rep. Prog. Phys.* **9** (1943) 256.
[17] W. H. Zachariasen, *Phys. Rev.* **57** (1940) 597; *Phys. Rev.*, **59** (1941) 766.
[18] P. Olmer, *Acta Cryst.* **1** (1948) 57; *Bull. Soc. Franç. Minér.* **71** (1948) 145.
[19] H. Curien, *Acta Cryst*. **5**(1952) 393.
[20] H. Cole and B. E. Warren, *J. Appl. Phys.* **23**(1952) 335.
[21] H. Cole, *J. Appl. Phys*. **24**(1953) 482.
[22] R.E. Joynson, *Phys. Rev.* **94** (1954) 851.
[23] E.H. Jacobsen, *Phys. Rev.*, **97** (1955) 654.
[24] C.B. Walker, *Phys. Rev.* **103** (1956) 547.
[25] N. Boccara, *C. R. Acad. Sci.* **250** (1960) 1025.
[26] W.J.L. Buyers and T. Smith, *Phys. Rev.* **150** (1966) 758.
[27] R. Colella and B.W. Batterman, *Phys. Rev. B* **1** (1970) 3913.
[28] N.S. Orlova, *Phys. Stat. Sol.* B **93** (1979) 503; *ibid.* **103** (1981) 115; *ibid*. **119** (1983) 541.
[29] N.N. Sirota and N.S. Orlova, *Doklady Akademii Nauk Belarusi* **33** (1989) 110.
[30] Z. Wu, H. Hong, R. Aburano, P. Zschack, P. Jemian, J. Tischler, H. Chen, D.-A. Luh, and T.-C. Chiang, *Phys. Rev. B* **59** (1999) 3283.
[31] J. Hastings, unpublished.
[32] M. Holt, Z. Wu, H. Hong, P. Zschack, P. Jemian, J. Tischler, H. Chen, and T.-C. Chiang, *Phys. Rev. Lett.* **83** (1999) 3317.
[33] M. Y. Chou and M. Choi, *Phys. Rev. Lett.* **84** (2000) 3733; M. Holt and T.-C. Chiang, *ibid.* **84** (2000) 3734.
[34] M. Holt, P. Czoschke, H. Hong, P. Zschack, H. K. Birnbaum and T.-C. Chiang, *Phys. Rev. B* **66** (2002) 064303.
[35] J. Wong, M. Wall, A. J. Schwartz, R. Xu, M. Holt, H. Hong, P. Zschack, and T.-C. Chiang, *Appl. Phys. Lett.* **84** (2004) 3747.
[36] M. Holt, P. Zschack, H. Hong, M.Y. Chou, and T.-C. Chiang, *Phys. Rev. Lett.* **86** (2001) 3799.
[37] M. Holt, M. Sutton, P. Zschack, H. Hong, and T.-C Chiang, *Phys. Rev. Lett.* **98** (2007) 065501.

2 Theory

2.1 X-ray scattering by matter

Discussions of the classical theory of x-ray scattering by matter usually begin with the elementary case of scattering by a single electron in free space, i.e., the Thomson scattering; the scattering by more complex systems such as atoms or solids are then formulated as coherent constructions by the scattering of individual electrons. This theory is both straightforward and successful in explaining various experimental observations. However, considering the quantum nature of the electron's motion, the classical picture is more of a successful model than a rigorous theory, as it neglects some fundamental difference between the physics of scattering by free-electrons and by macroscopic systems. More specifically, rigorously speaking, the process of a photon scattered by a free electron is always Compton scattering, i.e., an inelastic process that involves recoiling of the electron in free space; while according to a fundamental statement of quantum mechanics, scattering is only coherent if it is elastic (see §2.1.1.C below). It is therefore an interesting question why the observed x-ray intensities can be explained as coherent constructions from individual electrons. Moreover, scattering of x-rays by macroscopic materials is always observed to contain both elastic and inelastic intensities, commonly referred as Rayleigh scattering and Compton scattering, respectively. The origin of this elastic-inelastic split is not explained by the classical scattering theory either. In this section we will try to clarify these issues together with the applicability of the classical model while developing step-by-step the general theory of x-ray scattering

based on quantum mechanics. We shall begin with a brief review on the general formalism of light scattering.

2.1.1 General Formalism

2.1.1.A. Classical theory

The scattering of light by a charged particle may be treated based on classical electrodynamics. Consider the particle being driven into oscillation by the electric field of the incident light wave; the oscillating charge will then emit radiations into all directions in space which become the scattered light waves. The differential cross section for such a process is derived to be [1]

$$\frac{d\sigma}{d\Omega} = r_0^2 \cos^2 \Theta , \tag{2.1}$$

which is the Thomson scattering formula. Here Θ represents the angle between the polarization of the incident and outgoing waves, and is determined purely by geometry, while $r_0 = e^2 / 4\pi\varepsilon_0 mc^2$ is called the *scattering length* of the particle. For electrons, $r_0 \approx 2.82 \times 10^{-15}\,\mathrm{m}$ and is known as the *classical electron radius*. The scattering length represents a particle's scattering power; it is also equivalent here to the scattering amplitude as the scattered intensity is proportional to its square.

The next important assumption in the classical theory is that the scattering by a group of particles is a coherent sum over the scattering by the individuals, namely,

$$\frac{d\sigma}{d\Omega} = \left| \sum_i f_i e^{i(\mathbf{k}-\mathbf{k}')\cdot \mathbf{r}_i} \right|^2 \cos^2 \Theta , \tag{2.2}$$

where $\mathbf{k}$ and $\mathbf{k}'$ are the wavevectors of the incident and outgoing light, $\mathbf{r}_i$ and f_i are the position vector and scattering length for the *i*-th particle, respectively. The factor $e^{i(\mathbf{k}-\mathbf{k}')\cdot \mathbf{r}_i}$ is important as it reflects the phase difference between the scattered waves from different scattering centers in space and should be considered part of the scattering

amplitude.

2.1.1.B. Quantum theory

Before discussing the quantum scattering theory, we should first quantize the electromagnetic radiation, which is done by writing the vector potential **A** as

$$\mathbf{A} = \frac{c}{\sqrt{V}} \sum_{\mathbf{k},\alpha} \sqrt{\frac{\mu_0 \hbar}{2\omega}} \left(a_{\mathbf{k},\alpha} \mathbf{e}_\alpha e^{i\mathbf{k}\cdot\mathbf{r}} + a^\dagger_{\mathbf{k},\alpha} \mathbf{e}_\alpha e^{-i\mathbf{k}\cdot\mathbf{r}} \right), \tag{2.3}$$

where $\mathbf{e}_\alpha$ is the polarization vector with index α indicating one of the two possible polarizations for any specific wavevector **k**, $a^\dagger_{\mathbf{k},\alpha}$ and $a_{\mathbf{k},\alpha}$ are the photon creation and annihilation operators, respectively; $\omega = kc$ is the photon frequency while *V* is just a volume introduced for normalization.

For x-ray scattering, a non-relativistic approach should be sufficient in most cases as the photon energy is typically at the order of keV which is much less than the rest mass of electrons or atoms. Consider a single particle, for example, the Hamiltonian of the scattering process is

$$\begin{aligned} H &= \frac{1}{2m}\left(\mathbf{p} - e\mathbf{A}\right)^2 + V\left(\mathbf{r}\right) \\ &= \underbrace{\frac{\mathbf{p}^2}{2m} + V\left(\mathbf{r}\right)}_{H_0} - \underbrace{\frac{e}{2m}\left(\mathbf{p}\cdot\mathbf{A} + \mathbf{A}\cdot\mathbf{p}\right)}_{H^{(1)}_{\mathrm{int}}} + \underbrace{\frac{e^2\mathbf{A}^2}{2m}}_{H^{(2)}_{\mathrm{int}}}. \\ &\equiv \end{aligned} \tag{2.4}$$

The interaction terms $H^{(1)}_{\mathrm{int}}$ and $H^{(2)}_{\mathrm{int}}$ represent two different types of process. To first-order perturbation, only $H^{(2)}_{\mathrm{int}}$ is related to scattering, while $H^{(1)}_{\mathrm{int}}$ is the term related to photon emission and absorptions. Although $H^{(1)}_{\mathrm{int}}$ does contribute to scattering in the second-order perturbation, it is only significant when the photon energy is close to a resonance. Here we will only keep the $H^{(2)}_{\mathrm{int}}$ term for simplicity.

Let the initial and final state of the quantum system be $|A\rangle$ and $|B\rangle$, and denote the incident and outgoing photon states with $|\mathbf{k}\alpha\rangle$ and $|\mathbf{k}'\alpha'\rangle$. According to the golden rule, the differential cross section can be written as [2]

$$\left(\frac{d^2\sigma}{d\Omega d(\hbar\omega')}\right)_{A\to B} = \frac{c}{V}\frac{2\pi}{\hbar}\rho_{\hbar\omega',d\Omega}\left|\langle B,\mathbf{k}'\alpha'|H_{\text{int}}^{(2)}|A,\mathbf{k}\alpha\rangle\right|^2\delta\left(E_A+\hbar\omega-E_B-\hbar\omega'\right), \quad (2.5)$$

where $\rho_{\hbar\omega',d\Omega}$ is the density of state for the outgoing photon. We may continue by writing $H_{\text{int}}^{(2)}$ explicitly in terms of the photon field operators, and get

$$\begin{aligned}\frac{d\sigma}{d\Omega} &= \frac{r_0^2}{4}\frac{\omega'}{\omega}\left(\mathbf{e}_\alpha\cdot\mathbf{e}_{\alpha'}\right)^2\left|\langle B,\mathbf{k}'\alpha'|e^{i(\mathbf{k}-\mathbf{k}')\cdot\mathbf{r}}\left(a_{\mathbf{k}',\alpha'}^{+}a_{\mathbf{k},\alpha}+a_{\mathbf{k},\alpha}a_{\mathbf{k}',\alpha'}^{+}\right)|A,\mathbf{k}\alpha\rangle\right|^2 \\ &= r_0^2\frac{\omega'}{\omega}\left(\mathbf{e}_\alpha\cdot\mathbf{e}_{\alpha'}\right)^2\left|\langle B|e^{-i\mathbf{q}\cdot\mathbf{r}}|A\rangle\right|^2 ,\end{aligned} \quad (2.6)$$

where we have also integrated over the outgoing photon's energy, and the energy conservation will be assumed by default. Vector $\mathbf{q}$ is defined to be $\mathbf{k}'-\mathbf{k}$, and is often referred as the *scattering vector*.

2.1.1.C. Coherence of scattering

The statement that scattering is only coherent if it is elastic is often seen without a proof, or sometimes drawn from arguments based on the arbitrariness of the phase factor associated to the quantum state of the scattering system [3]. Here we provide an alternative proof that does not necessarily require this assumption.

Consider scattering from two quantum systems, coherence of the scattering is defined based on whether the total intensity, or cross section, can be expressed in one of these two forms:

$$\frac{d\sigma}{d\Omega}\propto\begin{cases}\left|f_1+f_2\right|^2 & \text{(coherent)}\\ \left|f_1\right|^2+\left|f_2\right|^2 & \text{(incoherent)}\end{cases},$$

where f_1 and f_2 are scattering amplitudes from the two systems, respectively. For

simplicity, we assume the two systems be composed with non-identical particles, and each has two quantum states of $|A\rangle$ and $|B\rangle$ only; we will use $|A\rangle_\alpha$ $(\alpha = 1,2)$ to denote the state of system α.

The cross section for a single system to scatter a photon while making a transition from $|\Lambda\rangle$ to $|\Lambda'\rangle$ $(\Lambda, \Lambda' = A \text{ or } B)$ is, according to Eq. (2.6),

$$\frac{d\sigma}{d\Omega} \propto \left|\langle \Lambda' | e^{-i\mathbf{q}\cdot\mathbf{r}} | \Lambda \rangle\right|^2 \equiv \left| f_{\Lambda\Lambda'} \right|^2, \tag{2.7}$$

where we have omitted other unrelated factors in the expression, $f_{\Lambda\Lambda'}$ is the scattering amplitude. The scattering involves a shift in photon frequency of $\omega' - \omega = (E_A - E_B)/\hbar$.

Now let's consider the two systems together as a larger system. The quantum state of the new system may therefore be denoted as $|\Lambda_1\rangle_1 |\Lambda_2\rangle_2$. The Hamiltonian should now be a simple sum of the two subsystems, and the cross section of any scattering should be given by

$$\frac{d\sigma}{d\Omega} \propto \left|\langle \Lambda_2' |_2 \langle \Lambda_1' |_1 \left(e^{-i\mathbf{q}\cdot\mathbf{r}_1} + e^{-i\mathbf{q}\cdot\mathbf{r}_2}\right) |\Lambda_1\rangle_1 |\Lambda_2\rangle_2 \right|^2. \tag{2.8}$$

Assume the system's initial state being $|A\rangle_1 |A\rangle_2$ before a scattering event. If elastic scattering is observed, it would be trivial to declare that the final state should still be $|A\rangle_1 |A\rangle_2$. However, if one observe an inelastic scattering event with $\Delta\omega = (E_A - E_B)/\hbar$, then the final state could be either one of the two possibilities:

$$|A\rangle_1 |A\rangle_2 \xrightarrow{\Delta\omega = (E_A - E_B)/\hbar} \begin{cases} |B\rangle_1 |A\rangle_2 \\ |A\rangle_1 |B\rangle_2 \end{cases}$$

Namely, the photon could have been scattered by either of the two subsystems. Notice that the situation does not correspond to particle exchange as we are assuming nonidentical particles. These are simply two orthogonal but degenerate states of the entire system. The total probability of such a process is therefore the sum of the probabilities of

the system making transitions into each one of these possible final states. Hence according to Eq. (2.8) we have

$$\begin{aligned}\left(\frac{d\sigma}{d\Omega}\right)_{\substack{A\to B\\ \text{total}}} &= \left(\frac{d\sigma}{d\Omega}\right)_{AA\to BA} + \left(\frac{d\sigma}{d\Omega}\right)_{AA\to AB} \\ &\propto \left|\langle A|_2 \langle B|_1 \left(e^{-i\mathbf{q}\cdot\mathbf{r}_1} + e^{-i\mathbf{q}\cdot\mathbf{r}_2}\right)|A\rangle_1 |A\rangle_2\right|^2 + \left|\langle B|_2 \langle A|_1 \left(e^{-i\mathbf{q}\cdot\mathbf{r}_1} + e^{-i\mathbf{q}\cdot\mathbf{r}_2}\right)|A\rangle_1 |A\rangle_2\right|^2 \\ &\propto \left|\langle B|e^{-i\mathbf{q}\cdot\mathbf{r}_1}|A\rangle_1 \langle A|A\rangle_2 + \langle B|A\rangle_1 \langle A|e^{-i\mathbf{q}\cdot\mathbf{r}_2}|A\rangle_2\right|^2 \\ &\quad + \left|\langle A|e^{-i\mathbf{q}\cdot\mathbf{r}_1}|A\rangle_1 \langle B|A\rangle_2 + \langle A|A\rangle_1 \langle B|e^{-i\mathbf{q}\cdot\mathbf{r}_2}|A\rangle_2\right|^2 .\end{aligned}$$

Since $\langle B|A\rangle_\alpha = 0$, we get the following equation:

$$\left(\frac{d\sigma}{d\Omega}\right)_{\substack{A\to B\\ \text{total}}} \propto |f_{BA1}|^2 + |f_{BA2}|^2 , \tag{2.9}$$

which represents a incoherent sum over the two subsystems, namely, the scattering is incoherent.

In contrast, if the scattering is elastic, we have only one possible final state, and

$$\begin{aligned}\left(\frac{d\sigma}{d\Omega}\right)_{\substack{A\to A\\ \text{total}}} &\propto \left|\langle A|_2 \langle A|_1 \left(e^{-i\mathbf{q}\cdot\mathbf{r}_1} + e^{-i\mathbf{q}\cdot\mathbf{r}_2}\right)|A\rangle_1 |A\rangle_2\right|^2 \\ &\propto |f_{AA1} + f_{AA2}|^2 .\end{aligned} \tag{2.10}$$

The scattering is now coherent. This completes the proof.

Although we have assumed nonidentical particles for simplicity, the derivation may be similarly worked out for identical particles. According to the above arguments, the essential aspect in determining the coherence of scattering is not the shift in photon energy, but the change in the quantum state of the scatterer. If $|A\rangle$ and $|B\rangle$ are degenerate states, for example, all scattering will appear elastic in energy, but only the one that does not involve a transition between the states would be coherent.

We shall now investigate scattering by different physical systems based on the general theories developed above, starting from the simplest case of a single electron.

2.1.2 Scattering by a single electron

Three different but related situations should be examined for a complete picture of single-electron scattering: a free electron, a recoilless electron in free space, and an electron bound in a potential. Comparison between their results will provide useful insights to the x-ray scattering processes in general.

2.1.2.A. Free electron

Scattering of photons by a free electron may be rigorously treated with relativistic quantum theory; the result is known as the Klein-Nishina formula [2,4]:

$$\left(\frac{d\sigma}{d\Omega}\right)_{\substack{\text{free electron}\\ \text{Compton}}} = \frac{r_0^2}{4}\left(\frac{\omega'}{\omega}\right)^2\left(\frac{\omega}{\omega'}+\frac{\omega'}{\omega}-2+4\cos^2\Theta\right), \tag{2.11}$$

where ω' is given by

$$\omega' = \frac{\omega}{1+\frac{\hbar\omega}{m_e c^2}\left(1-\cos 2\theta\right)}, \tag{2.12}$$

with 2θ being the scattering angle (notation in accordance with the convention of x-ray crystallography). For an x-ray photon of $\hbar\omega = 25$ keV and scattering angle $2\theta = 90°$, the frequency shift is ~5%, or ~1.2 keV.

The scattering is inelastic, and is hence incoherent.

2.1.2.B. Recoilless electron

In the hypothetical situation that the electron does not recoil in space, the scattering will become elastic. The cross section may be obtained from the Klein-Nishina formula (Eq. (2.11)) by taking the limit of $\omega' = \omega$:

$$\frac{d\sigma}{d\Omega} = \frac{r_0^2}{4}\left(\frac{\omega}{\omega}\right)^2\left(\frac{\omega}{\omega}+\frac{\omega}{\omega}-2+4\cos^2\Theta\right) = r_0^2\cos^2\Theta. \tag{2.13}$$

This is just the classical Thomson scattering formula (Eq. (2.2)). Hence for single

electron scattering the quantum mechanical result coincides with the classical one at the recoilless limit, and it is only at this limit that the scattering from different electrons would become coherent.

2.1.2.C. Bound Electron

If the electron is in a bound state in a potential $V(r)$, then due to the confinement of the potential, which is assumed to be fixed in space, the electron will no longer recoil; instead it may end up in one of the eigenstates determined by $V(r)$. Therefore depending on the final state, the scattering may be either elastic or inelastic.

(i) *Elastic (coherent) scattering*. If the electron remains at its initial state $|A\rangle$, the scattering is elastic. The cross section can be derived to be

$$\begin{aligned}\left(\frac{d\sigma}{d\Omega}\right)_{\text{elastic}} &= r_0^2\left(\mathbf{e}_\alpha\cdot\mathbf{e}_{\alpha'}\right)^2\left|\langle A|e^{-i\mathbf{q}\cdot\mathbf{r}}|A\rangle\right|^2 \\ &= \left(\frac{d\sigma}{d\Omega}\right)_{\text{Thomson}}\left|\int e^{-i\mathbf{q}\cdot\mathbf{r}}\rho_A(\mathbf{r})\,d^3\mathbf{r}\right|^2 \\ &= \left(\frac{d\sigma}{d\Omega}\right)_{\text{Thomson}}\left|f^{(\mathrm{e})}\right|^2,\end{aligned} \tag{2.14}$$

where $\rho_A(\mathbf{r})$ is the electron's probability density at state $|A\rangle$, and the *single electron form factor* $f^{(\mathrm{e})}$ is defined as

$$f^{(\mathrm{e})} \equiv \int e^{i(\mathbf{k}-\mathbf{k}')\cdot\mathbf{r}}\rho_A(\mathbf{r})\,d^3\mathbf{r}\,. \tag{2.15}$$

Notice that the result simply reduces to the Thomson scattering formula at the limit of $\rho_A(\mathbf{r})=\delta(\mathbf{r})$, i.e., when the electron is "point-like" with a negligible extent of spatial distribution. In general, the expression is formally a coherent construction of Thomson scattering by a continuous charge distribution of $e\rho_A(\mathbf{r})$ in space, which interestingly coincides with the classical picture of scattering. This coincidence, together with the

correctness for the Thomson scattering formula in predicting the scattering cross section of a recoilless electron, is the fundamental reason for the wide applicability of the classical x-ray scattering theory.

(ii) *Inelastic (incoherent) scattering*. The scattering is inelastic if the final state $|B\rangle \neq |A\rangle$. The total inelastic cross section is given by a sum over all possible final states:

$$\left(\frac{d\sigma}{d\Omega}\right)_{\text{inelastic}} = r_0^2 \left(\mathbf{e}_\alpha \cdot \mathbf{e}_{\alpha'}\right)^2 \sum_B^{(B\neq A)} \frac{\omega'}{\omega} \left|\langle B| e^{i(\mathbf{k}-\mathbf{k}')\cdot\mathbf{r}} |A\rangle\right|^2 . \tag{2.16}$$

In case the energy shift is small compared to the photon energy, we may assume $\omega'/\omega \approx 1$ and get

$$\begin{aligned}\left(\frac{d\sigma}{d\Omega}\right)_{\text{inelastic}} &= r_0^2 \left(\mathbf{e}_\alpha \cdot \mathbf{e}_{\alpha'}\right)^2 \sum_B^{(B\neq A)} \langle A| e^{i(\mathbf{k}'-\mathbf{k})\cdot\mathbf{r}} |B\rangle\langle B| e^{i(\mathbf{k}-\mathbf{k}')\cdot\mathbf{r}} |A\rangle \\ &= \left(\frac{d\sigma}{d\Omega}\right)_{\text{Thomson}} \left\{ \sum_B^{\text{all states}} \langle A| e^{i(\mathbf{k}'-\mathbf{k})\cdot\mathbf{r}} |B\rangle\langle B| e^{i(\mathbf{k}-\mathbf{k}')\cdot\mathbf{r}} |A\rangle \right. \\ &\qquad \left. - \langle A| e^{i(\mathbf{k}'-\mathbf{k})\cdot\mathbf{r}} |A\rangle\langle A| e^{i(\mathbf{k}-\mathbf{k}')\cdot\mathbf{r}} |A\rangle \right\} .\end{aligned}$$

Using the completeness property for the sum over *B*, we have

$$\left(\frac{d\sigma}{d\Omega}\right)_{\text{inelastic}} = \left(\frac{d\sigma}{d\Omega}\right)_{\text{Thomson}} \left(1 - \left|f^{(e)}\right|^2\right). \tag{2.17}$$

Comparing with Eq. (2.14) we have the single-electron sum rule:

$$\left(\frac{d\sigma}{d\Omega}\right)_{\text{inelastic}} + \left(\frac{d\sigma}{d\Omega}\right)_{\text{elastic}} = \left(\frac{d\sigma}{d\Omega}\right)_{\text{Thomson}} . \tag{2.18}$$

Therefore it appears as if the total cross section is just redistributed into the different channels of elastic and inelastic processes.

The electron, together with the potential $V(r)$, form a scattering system that is different from a single free electron. First of all, this system does not recoil as $V(r)$ is fixed in space, which makes it possible for the scattering to be purely elastic. Secondly, the system has an internal degree of freedom which is the electron's quantum state; and it

is this possibility of an internal transition that has given rise to the elastic-inelastic split in the observed intensities. Had the electron have any internal structure of itself that may couple with the electromagnetic field, we would have observed such a split in the free electron scatterings as well.

2.1.3 Scattering by an atom

When discussing the x-ray scattering by atoms it is a common practice to ignore the contribution from the nuclei, due to their much smaller cross section compared to the electrons. More specifically, we may write down the Thomson scattering cross section for a nucleus with atomic number Z and mass M as

$$\begin{aligned}\left(\frac{d\sigma}{d\Omega}\right)_{\text{nucleus}} &= \frac{Z^2e^2}{4\pi\varepsilon_0 Mc^2}\cos^2\Theta \\ &= \frac{Z^2 m_e}{M}\cdot\left(\frac{d\sigma}{d\Omega}\right)_{\text{electron}}\end{aligned}, \tag{2.19}$$

where m_e/M may be estimated as 1/(2Z×1800). Ratio of the scattering power of a nucleus to an electron is therefore ~Z/3600. Since there are Z electrons per atom, the error introduced by ignoring the nuclei's contribution during an x-ray scattering process is indeed marginal, and it usually falls well below the typical noise levels in x-ray intensity measurements.

With the nucleus ignored, the previously discussed case of a bound electron basically corresponds to a single-electron atom that does not recoil in space. In general, the recoil of atoms upon scattering off an x-ray photon is little compared to electrons due to their larger mass. As an example, when an ^{16}O atom scatters a 25 keV photon into an angle of $2\theta = 90°$ in free space, without any electronic excitations, the scattered photon will have an energy loss of ~ 42 meV, roughly one millionth of the incident photon's energy. Such a small shift, however, is still well detectible with modern experimental techniques; therefore depending on the context of the discussion, it may not always be ignored. – We

shall first examine the case of a recoilless atom.

2.1.3.A. Recoilless atom

For a multi-electron atom with its nucleus fixed in space, we may follow the same treatment as the single bound electron. The scattering term in the Hamiltonian should now be written as

$$H_{\text{int}}^{(2)} = \frac{e^2}{2m}\sum_{i=1}^{n}\mathbf{A}\left(\mathbf{r}_i\right)^2 \tag{2.20}$$

where *n* is the number of electrons. The elastic cross section is therefore

$$\left(\frac{d\sigma}{d\Omega}\right)_{\substack{\text{single atom}\\ \text{elastic}}} = r_0^2\left(\mathbf{e}_\alpha\cdot\mathbf{e}_{\alpha'}\right)^2\left|\left\langle A\left|\sum_{i=1}^{n}e^{-i\mathbf{q}\cdot\mathbf{r}_i}\right|A\right\rangle\right|^2 \tag{2.21}$$

for the initial electronic state of $\left|A\right\rangle$. We may further adopt the independent electron approximation and write the wavefunction of $\left|A\right\rangle$ as an antisymmetric combination of single electron wavefunctions:

$$\psi_A = \frac{1}{\sqrt{n!}}\mathcal{A}\left[\psi_1\left(\mathbf{r}_1\right)\psi_2\left(\mathbf{r}_2\right)\cdots\psi_n\left(\mathbf{r}_n\right)\right], \tag{2.22}$$

with $\mathcal{A}$ being the antisymmetrizing operator. Substitute Eq. (2.22) into Eq. (2.21), we have

$$\begin{aligned}\left(\frac{d\sigma}{d\Omega}\right)_{\substack{\text{single atom}\\ \text{elastic}}} &= \left(\frac{d\sigma}{d\Omega}\right)_{\text{Thomson}}\left|\sum_{i=1}^{n}\int e^{-i\mathbf{q}\cdot\mathbf{r}}\rho_i\left(\mathbf{r}\right)d^3\mathbf{r}\right|^2\\ &= \left(\frac{d\sigma}{d\Omega}\right)_{\text{Thomson}}\left|\int e^{-i\mathbf{q}\cdot\mathbf{r}}\rho\left(\mathbf{r}\right)d^3\mathbf{r}\right|^2\\ \text{or} &= \left(\frac{d\sigma}{d\Omega}\right)_{\text{Thomson}}\left|\sum_{i=1}^{n}f_i^{(\text{e})}\right|^2,\end{aligned} \tag{2.23}$$

where *i* has become the index of single electron states instead of the electrons, ρ_i is the electron density for the *i*-th single electron state while ρ is the total electron density.

The cross section is more commonly known in the following form:

$$\left(\frac{d\sigma}{d\Omega}\right)_{\substack{\text{single atom}\\ \text{elastic}}} = \left(\frac{d\sigma}{d\Omega}\right)_{\text{Thomson}} \left| f^{(\mathrm{A})} \right|^2, \tag{2.24}$$

with the quantity $f^{(\mathrm{A})}$ defined as the *atomic form factor* (also called *atomic structure factor* or *atomic scattering factor*):

$$f^{(\mathrm{A})} \equiv \int e^{-i\mathbf{q}\cdot\mathbf{r}} \rho(\mathbf{r}) d^3\mathbf{r} = \sum_{i=1}^{n} f_i^{(\mathrm{e})}, \tag{2.25}$$

which is essentially the Fourier transform of the total electron density; meanwhile it also represents a coherent sum over the individual electrons, which is true since the scattering does not involve any electronic excitations.

The derivation of total inelastic cross section is more complex. Following the same steps that led to Eq. (2.17), we have

$$\begin{aligned}
\left(\frac{d\sigma}{d\Omega}\right)_{\substack{\text{single atom}\\ \text{inelastic}}} &= r_0^2 \left(\mathbf{e}_\alpha \cdot \mathbf{e}_{\alpha'}\right)^2 \left\{ \sum_{B}^{\text{all states}} \left\langle A \middle| \sum_{j=1} e^{i\mathbf{q}\cdot\mathbf{r}_j} \middle| B \right\rangle \left\langle B \middle| \sum_{i=1} e^{-i\mathbf{q}\cdot\mathbf{r}_i} \middle| A \right\rangle \right. \\
&\qquad \left. - \left\langle A \middle| \sum_{j=1} e^{i\mathbf{q}\cdot\mathbf{r}_j} \middle| A \right\rangle \left\langle A \middle| \sum_{i=1} e^{-i\mathbf{q}\cdot\mathbf{r}_i} \middle| A \right\rangle \right\} \\
&= \left(\frac{d\sigma}{d\Omega}\right)_{\text{Thomson}} \left\{ \left\langle A \middle| \sum_{i,j} e^{-i\mathbf{q}\cdot\left(\mathbf{r}_i - \mathbf{r}_j\right)} \middle| A \right\rangle - \left| f^{(\mathrm{A})} \right|^2 \right\} \\
&= \left(\frac{d\sigma}{d\Omega}\right)_{\text{Thomson}} \left\{ Z \langle A | A \rangle + \sum_{i \neq j} \left\langle A \middle| e^{-i\mathbf{q}\cdot\left(\mathbf{r}_i - \mathbf{r}_j\right)} \middle| A \right\rangle - \left| f^{(\mathrm{A})} \right|^2 \right\}.
\end{aligned} \tag{2.26}$$

The second term in the bracket can be further expanded if we write the total wavefunction in terms of single electron wavefunctions as in Eq. (2.22). Some simple derivations will lead us to

$$\sum_{i \neq j} \left\langle A \middle| e^{-i\mathbf{q}\cdot\left(\mathbf{r}_i - \mathbf{r}_j\right)} \middle| A \right\rangle = \frac{1}{2} \sum_{i \neq j} \left\{ f_i^{(\mathrm{e})} f_j^{(\mathrm{e})*} + f_j^{(\mathrm{e})} f_i^{(\mathrm{e})*} - f_{ji}^{(\mathrm{e})} f_{ji}^{(\mathrm{e})*} - f_{ij}^{(\mathrm{e})} f_{ij}^{(\mathrm{e})*} \right\}, \tag{2.27}$$

where the exchange term $f_{ij}^{(\mathrm{e})}$ is defined as

$$f_{ij}^{(\mathrm{e})} \equiv \int e^{-i\mathbf{q}\cdot\mathbf{r}} \psi_i(\mathbf{r}) \psi_j^*(\mathbf{r}) d^3\mathbf{r}, \tag{2.28}$$

Substitute Eq. (2.27) into Eq. (2.26) and write $f^{(\mathrm{A})}$ as a summation of single-electron form factors, eventually we have*

$$\left(\frac{d\sigma}{d\Omega}\right)_{\substack{\text{single atom}\\ \text{inelastic}}} = \left(\frac{d\sigma}{d\Omega}\right)_{\text{Thomson}} \left(Z - \sum_i \left| f_i^{(\mathrm{e})} \right|^2 - \sum_{i \neq j} \left| f_{ij}^{(\mathrm{e})} \right|^2 \right). \tag{2.29}$$

Comparing this result with the elastic cross section of Eq. (2.24), we see that the simple sum rule for the single-electron scattering (Eq. (2.18)) no longer holds in a multi-electron system. In practice, both elastic and inelastic scattering cross sections should be computed based on knowledge of the electronic wavefunctions, which one may obtain from first-principle calculations. The computed results have been tabulated and widely available in references [5,6]; although instead of cross sections, quantities usually listed are the atomic form factors $f^{(\mathrm{A})}$ (or simply f) and the *incoherent scattering functions S*. The latter is defined as follows [6,7]

$$\left(\frac{d\sigma}{d\Omega}\right)_{\substack{\text{single atom}\\ \text{inelastic}}} = \left(\frac{d\sigma}{d\Omega}\right)_{\substack{\text{single electron}\\ \text{Compton}}} \cdot S\left(\omega, 2\theta\right). \tag{2.30}$$

Both f and S are functions of the phonon frequency and the scattering angle only, due to the spherical symmetry of the atom.

2.1.3.B. Free atom

For a full treatment of the atom including its translational motion space, we may write the total wavefunction as

$$\Psi = \phi(\mathbf{R})\psi(\tilde{\mathbf{r}}_1, \ldots, \tilde{\mathbf{r}}_n), \tag{2.31}$$

where $\mathbf{R}$ and $\phi(\mathbf{R})$ are the position vector and wavefunction of the nucleus, respectively, while $\tilde{\mathbf{r}}_i \equiv \mathbf{r}_i - \mathbf{R}$ are the relative positions of the electrons to the nucleus. In

* The same formula is given in Ref.[5] (equation 6.1.1.11) with an error of $f_{j,k}$ missing a second power.

free space the eigenfunctions of $\phi(\mathbf{R})$ should take the form of plane waves characterized by the momentum **p**. Hence together with the radiation field, the initial and final state of the system may be written as $|\mathbf{p}, A, \mathbf{k}\alpha\rangle$ and $|\mathbf{p}', B, \mathbf{k}'\alpha'\rangle$. Cross section for this particular transition is then

$$\left(\frac{d\sigma}{d\Omega}\right)_{\substack{\text{free atom}\\A\to B}} = r_0^2 \frac{\omega'}{\omega}\left(\mathbf{e}_\alpha \cdot \mathbf{e}_{\alpha'}\right)^2 \left|\langle \mathbf{p}', B| \sum_{i=1}^{n} e^{-i\mathbf{q}\cdot\mathbf{r}_i} |\mathbf{p}, A\rangle\right|^2 . \tag{2.32}$$

Substituting $\mathbf{r}_i$ with $\tilde{\mathbf{r}}_i + \mathbf{R}$, we have

$$\begin{aligned}\left(\frac{d\sigma}{d\Omega}\right)_{\substack{\text{free atom}\\A\to B}} &= r_0^2 \frac{\omega'}{\omega}\left(\mathbf{e}_\alpha \cdot \mathbf{e}_{\alpha'}\right)^2 \left|\langle \mathbf{p}'| e^{-i\mathbf{q}\cdot\mathbf{R}} |\mathbf{p}\rangle \langle B| \sum_{i=1}^{n} e^{-i\mathbf{q}\cdot\tilde{\mathbf{r}}_i} |A\rangle\right|^2 \\ &= \left(\frac{d\sigma}{d\Omega}\right)_{\substack{\text{recoilless atom}\\A\to B}} \delta\left(\mathbf{p} - \mathbf{p}' - \hbar\mathbf{q}\right) ,\end{aligned} \tag{2.33}$$

The result is therefore the same as the recoilless case; thus both Eq. (2.23) and Eq. (2.29) should still hold for a free atom. Although energy of the scattered photon is now changed due to the recoil, the energy shift of an x-ray photon is rather small compared to typical electronic excitations and we can still distinguish between the original elastic and inelastic channels; yet rigorously speaking, the former should now be more appropriately referred to as "quasielastic" instead.

Care should be taken to speak of whether the quasielastic scattering is coherent or not. Literally, the answer to this question should be no, as the scattering from different atoms are always incoherent as it is no longer elastic. However, mathematically the quasielastic intensity from a single atom may still be computed according to Eq. (2.23) as a coherent construction of the individual electrons. This is because the scattering does not involve any excitation in the electronic degrees of freedom within the atom; while the only degree of freedom that is perturbed during the process, i.e., the translation of the nucleus, is independent of the motions of the electrons. Nonetheless, the coherence only

exists between electrons within the same atom. As a result, scattering of x-ray by a gas should always be computed as an incoherent sum over the constituent atoms (or molecules). Scattering by a solid, on the other hand, is more complicated.

2.1.4 Scattering by a solid

A solid-atom-electron hierarchy is usually assumed when discussing the x-ray scattering by a solid material; namely, the electrons are considered to be affiliated to individual atoms and moves rigidly with the nuclei. This may not be a good approximation for the valence electrons, but the deviation is minor in terms of the electron density, and is usually neglected in the treatment of elastic scatterings.

The recoil of any macroscopic object when scattering off a photon is infinitesimal and can be comfortably neglected. Analogy may therefore be drawn between a solid and a recoilless multi-electron atom, in the sense that a solid may be regarded as the bound state of a large number of atoms, glued together by the interatomic potential; while the different electronic eigenstates in an atom may be compared to the different state of atomic motions, i.e., lattice vibrations in a crystal. Therefore, just like the elastic scattering from an atom is coherently constructed by the electrons, the elastic scattering from a solid should be a coherent summation over the scattering from the atoms. Unlike the electrons, however, atoms are particles with intrinsic degrees of freedom, and their scatterings contain both elastic and inelastic intensities, among them only the coherent (elastic) part should participate in the aforementioned summation. Thus, analogous to Eq. (2.23), we may write

$$\left(\frac{d\sigma}{d\Omega}\right)_{\substack{\text{solid}\\ \text{elastic}}} = r_0^2 \left(\mathbf{e}_\alpha \cdot \mathbf{e}_{\alpha'}\right)^2 \left| \sum_l f_l^{(\mathrm{A})} \int e^{-i\mathbf{q}\cdot\mathbf{r}_l} \rho\left(\mathbf{r}_l\right) d^3\mathbf{r}_l \right|^2 , \tag{2.34}$$

where l is the index for the atoms, $\mathbf{r}_l$ is the atom's position, and $\rho\left(\mathbf{r}_l\right)$ is the density distribution of the atom in space. If the thermal vibration of the atoms are neglected, we

may write $\rho(\mathbf{r}_l) = \delta(\mathbf{r}_l - \mathbf{R}_l)$, with $\mathbf{R}_l$ being the equilibrium positions, and the expression will reduce to

$$\left(\frac{d\sigma}{d\Omega}\right)_{\substack{\text{solid}\\ \text{elastic}}} = r_0^2 \left(\mathbf{e}_\alpha \cdot \mathbf{e}_{\alpha'}\right)^2 \left| \sum_l f_l^{(\mathrm{A})} e^{-i\mathbf{q}\cdot\mathbf{R}_l} \right|^2 , \tag{2.35}$$

which is exactly the classical x-ray scattering formula of Eq. (2.2). The summation in Eq. (2.35) is called the structural factor of the solid. For a perfect crystal without lattice vibrations, Eq. (2.35) will simply give rise to the Bragg peaks.

If the lattice vibration is not ignored, however, the deviation of $\rho(\mathbf{r}_l)$ from pure δ-functions will lead to the concept of Debye-Waller factors, which will be introduced later in §2.3.

The inelastic scattering is more complicated, as it may arise from at least two different types of excitations: the collective motion of the atoms as the lattice vibration, and transitions in the electronic states within each atom (if electrons are considered to be always affiliated to individual atoms). The latter is commonly referred as Compton scattering. Unlike the elastic scattering, its intensity should be a simple sum over the inelastic scattering intensities from the individual atoms due to its incoherent nature. This may not hold exactly for real solids, however, as the electrons become itinerant upon bonding and their wavefunctions may deviate substantially from the states in single atoms, especially for the valence electrons.

The inelastic scattering by the thermal vibration of the atoms is just the thermal diffuse scattering (TDS) when referred from another perspective. The energy shift is usually at the order of meV, which is similar to the quasielastic scattering of free atoms discussed in §2.1.3.B. However, there is still a fundamental difference between these two types of processes, as the energy loss due to a free atom's recoil is dependent on the frequency of the incident photon, while in a solid the energy shift is purely determined by the frequency of the lattice normal modes.

Interestingly, although according to our discussions, the classical scattering theory should only be applicable to the coherent elastic scattering by the solid, it has been proved that the classical approach can give an accurate estimation of the total intensity of TDS as well, if assisted with some quantum statistics [8]. We shall not enter the elaborate details in proving the mathematical equivalence of the classical and quantum treatments on this problem. But briefly, their equivalence arises from the following reasons: i) the motion of the electrons and the nuclei in a solid can be effectively separated in most cases, and the scattering does not involve any excitation in the electronic degrees of freedom; ii) the electronic density in a solid may be well approximated as a simple sum of overlapping atomic spheres; iii) the relative frequency change $\Delta\omega/\omega$ during the scattering is negligible for x-ray photons; iv) the lattice vibrations are largely harmonic, thus the wavelengths and frequencies of the normal modes can be accurately predicted by the classical theory, although quantum statistics has to be brought in for a good estimation of the thermal average of the amplitudes.

We will adopt the classical approach, which is mathematically more straightforward, in developing the formulary of lattice dynamics and the theory of x-ray TDS.

2.2 Phonons

"Phonon" is the name given to the elementary excitation in a solid that corresponds to the collective motion of atomic nuclei around their equilibrium positions. Theoretically, the concept implies the fundamental assumption of the Born-Oppenheimer approximation, i.e., the dynamics of the nuclei and the electrons in a system may be treated separately due to the orders-of-magnitude difference between their mass [9]; this leads to the auxiliary concept of the potential energy surface (PES), which neglects the relatively slow motion of the nuclei and describes the total energy of the system as a function of the

nuclei's positions only. The PES is a manifestation of the electronic structure of the system and can usually be regarded as an effective potential field that the nuclei move within. At the vicinity of the equilibrium, the PES is approximately quadratic, and motion of the nuclei may be treated as a multi-dimensional harmonic oscillator, with the elementary quanta of the normal modes named phonons. The anharmonic terms in the PES are usually present but not dominant in a real system, and may be accounted for perturbatively in terms of phonon-phonon interactions. While in situations when the Born-Oppenheimer approximation is no longer accurate, the motions of the electrons and the nuclei should be treated interactively, which is usually done based on the concept of electron-phonon coupling. – Research described in this dissertation primarily focus on determination of the frequencies of the lattice normal modes, and we will assume the harmonic approximation to all crystal potentials.

We will be following the classical approach, or more precisely, a "semiclassical" one for treatment of the lattice dynamics before developing the TDS theory in §2.3. Here "semiclassical" refers to solving the atomic motions with classical mechanics while the thermal averages of their vibrational amplitudes are determined according to quantum statistics. For complete quantum mechanical treatment of this problem, one may refer to the books by Born and Huang [10] and Marder [11].

Some basic notations are defined as follows:

$\mathbf{R}_m$ = position vector of the of the m-th unit cell
$\boldsymbol{\tau}_s$ = basis vector of the s-th atom within a unit cell
$\mathbf{u}_{m,s}$ = displacement of the s-th atom in the m-th unit cell
μ_s = mass of the s-th atom
$\omega_{\mathbf{k},j}$ = angular frequency of the j-th phonon mode with wave vector $\mathbf{k}$
$\mathbf{e}_{\mathbf{k},j,s}$ = eigenvector associated with the s-th atom for phonon mode ($\mathbf{k}$, j)

The potential energy of the crystal about its equivalent configuration may be expanded in terms of the atomic displacements according to

$$U = U_0 + \frac{1}{2}\sum_{m,m'=1}^{N}\sum_{s,s'=1}^{n}\mathbf{u}_{m,s}\cdot\left.\frac{\partial^2 U}{\partial\mathbf{r}_{m,s}\partial\mathbf{r}_{m',s'}}\right|_{\substack{\mathbf{r}_{m,s}=\mathbf{R}_m+\boldsymbol{\tau}_s \\ \mathbf{r}_{m',s'}=\mathbf{R}_{m'}+\boldsymbol{\tau}_{s'}}}\cdot\mathbf{u}_{m',s'}+\ldots, \tag{2.36}$$

where *n* is the number of atoms per unit cell and *N* is the total number of unit cells within the crystal. The second-derivatives of the potential energy are related to the *Born-von Kármán (BvK) force constants* [12] with a negative sign:

$$\Phi^{\alpha,\beta}_{m,s,m',s'} = -\frac{\partial^2 U}{\partial r^{\alpha}_{m,s}\partial r^{\beta}_{m',s'}}, \tag{2.37}$$

with α and β denoting the Cartesian indices x, y, and z. Due to the translational symmetry of the crystal, $\Phi^{\alpha,\beta}_{m,s,m',s'}$ should be functions of $\mathbf{R}_{m'}-\mathbf{R}_m$ only. For convenience we will abbreviate $\mathbf{R}_{m'}-\mathbf{R}_m$ as $\mathbf{R}_{m,m'}$ hereafter.

The equation of motion of the individual atoms is therefore given by

$$\mu_s\frac{\mathrm{d}^2}{\mathrm{d}t^2}\mathbf{u}_{m,s} = \sum_{m',s'}\boldsymbol{\Phi}_{s,s'}\left(\mathbf{R}_{m,m'}\right)\cdot\mathbf{u}_{m',s'}\,. \tag{2.38}$$

where $\boldsymbol{\Phi}_{s,s'}\left(\mathbf{R}_{m,m'}\right)$ is a 3×3 force constant matrix. One seeks wave-like solutions to Eq. (2.38) in the form of:

$$\mathbf{u}_{m,s} = \mathrm{Re}\left[\frac{1}{\sqrt{\mu_s}}a_{\mathbf{k},j}\mathbf{e}_{\mathbf{k},j,s}\exp\left(i\mathbf{k}\cdot\mathbf{R}_m - i\omega_{\mathbf{k},j}t\right)\right]. \tag{2.39}$$

where **k** is the wavevector, *j* is an index for the normal modes, $a_{\mathbf{k},j}$ is the amplitude. Substitute Eq. (2.39) into Eq. (2.38) would lead to an eigenvalue equation:

$$\mathbf{D}\left(\mathbf{k}\right)\cdot\boldsymbol{\varepsilon}_{\mathbf{k},j} = \omega^2_{\mathbf{k},j}\boldsymbol{\varepsilon}_{\mathbf{k},j}\,. \tag{2.40}$$

The eigenvector $\boldsymbol{\varepsilon}_{\mathbf{k},j}$ has 3*n* components:

$$\boldsymbol{\varepsilon}_{\mathbf{k},j} \equiv \begin{pmatrix} \mathbf{e}_{\mathbf{k},j,s=1} \\ \mathbf{e}_{\mathbf{k},j,s=2} \\ \cdots \\ \mathbf{e}_{\mathbf{k},j,s=n} \end{pmatrix}, \tag{2.41}$$

which satisfy the relation of orthonormality:

$$\boldsymbol{\varepsilon}_{\mathbf{k},j} \cdot \boldsymbol{\varepsilon}^{*}_{\mathbf{k}',j'} = \sum_{s} \mathbf{e}_{\mathbf{k},j,s} \cdot \mathbf{e}^{*}_{\mathbf{k}',j',s} = \delta_{\mathbf{k},\mathbf{k}'}\delta_{j,j'} \,. \tag{2.42}$$

The matrix $\mathbf{D}(\mathbf{k})$ in Eq. (2.40), called the *dynamical matrix*, is defined as

$$D^{\alpha,\beta}_{s,s'}(\mathbf{k}) \equiv -\sum_{m'} \frac{\Phi^{\alpha,\beta}_{s,s'}(\mathbf{R}_{m,m'})}{\sqrt{\mu_s \mu_{s'}}} \exp\left(i\mathbf{k}\cdot\mathbf{R}_{m,m'}\right). \tag{2.43}$$

This definition of the dynamical matrix is periodic in reciprocal space. $\mathbf{D}(\mathbf{k})$ may also be defined as non-periodic if, instead of Eq. (2.39), we write the lattice wave in the form of

$$\mathbf{u}^{(np)}_{m,s}(t) = \mathrm{Re}\left\{ \frac{1}{\sqrt{\mu_s}} a_{\mathbf{k},j} \mathbf{e}^{(np)}_{\mathbf{k},j,s} \exp\left[i\left(\mathbf{k}\cdot(\mathbf{R}_m + \boldsymbol{\tau}_s) - \omega_{\mathbf{k},j} t\right)\right]\right\}, \tag{2.44}$$

with the atomic basis also included in the lattice Fourier transformation. The superscript (*np*) stands for non-periodic. The corresponding dynamical matrix is

$$D^{\alpha,\beta}_{s,s'}(\mathbf{k})^{(np)} \equiv -\sum_{m'} \frac{\Phi^{\alpha,\beta}_{s,s'}(\mathbf{R}_{m,m'})}{\sqrt{\mu_s \mu_{s'}}} \exp\left[i\mathbf{k}\cdot\left(\mathbf{R}_{m,m'} + \boldsymbol{\tau}_{s,s'}\right)\right], \tag{2.45}$$

where $\boldsymbol{\tau}_{s,s'}$ is the shorthand notation for $\boldsymbol{\tau}_{s'} - \boldsymbol{\tau}_s$.

Existence of the two definitions of the dynamical matrix could be a source of confusion. Although they would yield the same set of eigenvalues, there is a phase difference between their eigenvectors (superscript (*p*) stands for periodic):

$$\mathbf{e}^{(p)}_{\mathbf{k},j,s} = \mathbf{e}^{(np)}_{\mathbf{k},j,s} \exp\left(i\mathbf{k}\cdot\boldsymbol{\tau}_s\right). \tag{2.46}$$

Such a difference will also affect the final expression of TDS intensities. Care should be taken to make a clear distinction between the two definitions. We will be primarily using the periodic definition in our derivation, while some key formulae will also be presented with their non-periodic form.

Solving Eq. (2.40) is then the major step in the theoretical treatment of lattice vibrations within the harmonic approximation. It is an eigenvalue equation with dimension of 3*n*. For any wavevector $\mathbf{k}$, there are 3*n* eigenstates that correspond to 3*n* normal modes

of lattice waves, whose quantized elementary excitations are called phonons. The square root of the eigenvalues, $\omega_{\mathbf{k},j}$, are the phonon frequencies, and the functional dependence of $\omega_{\mathbf{k},j}$ on wavevector **k** in reciprocal space is referred to as the phonon dispersion relation. The phonon modes with the same wavevector **k** are usually distinguished by their eigenvectors, which represents the polarization of the atomic vibrations and are orthogonal to each other. When examined along a certain direction in the reciprocal space, the phonon modes with same polarization may be conceptually grouped together, referred to as a phonon branch.

The real displacement of an atom should consist of a superposition of all vibrational modes:

$$\mathbf{u}_{m,s} = \mathrm{Re}\left[\frac{1}{\sqrt{\mu_s}}\sum_{\mathbf{k},j} a_{\mathbf{k},j}\mathbf{e}_{\mathbf{k},j,s}\exp\left(i\mathbf{k}\cdot\mathbf{R}_m - i\omega_{\mathbf{k},j}t + i\varphi_{\mathbf{k},j}\right)\right], \tag{2.47}$$

with $\varphi_{\mathbf{k},j}$ being an arbitrary phase factor. The amplitude $a_{\mathbf{k},j}$ is the generalized coordinate for the normal mode (**k**, *j*), and may be defined as a real positive number, whose value, at thermal equilibrium, should be determined according to the statistical distribution of vibrational energies.

The mean kinetic energy of the harmonic system may be estimated with classical mechanics as

$$\begin{aligned}\langle KE\rangle &= \frac{1}{2}\sum_{m,s}\mu_s\left\langle\left(\frac{d\mathbf{u}_{m,s}}{dt}\right)^2\right\rangle \\ &= \frac{N}{4}\sum_{\mathbf{k},j}\left\langle a_{\mathbf{k},j}^2\right\rangle\omega_{\mathbf{k},j}^2\end{aligned}. \tag{2.48}$$

Meanwhile, quantum statistics gives the total energy of the system:

$$\langle E\rangle = 2\langle KE\rangle = \sum_{\mathbf{k},j}\hbar\omega_{\mathbf{k},j}\left(\frac{1}{e^{\hbar\omega_{\mathbf{k},j}/k_BT}-1}+\frac{1}{2}\right) \tag{2.49}$$

Comparing Eqs. (2.48) and (2.49), and assuming that each mode moves independently, we have

$$\begin{aligned}\left\langle a_{\mathbf{k},j}^2 \right\rangle &= \frac{2\hbar}{N\omega_{\mathbf{k},j}}\left(\frac{1}{e^{\hbar\omega_{\mathbf{k},j}/k_BT}-1}+\frac{1}{2}\right) \\ &= \frac{\hbar}{N\omega_{\mathbf{k},j}}\coth\left(\frac{\hbar\omega_{\mathbf{k},j}}{2k_BT}\right).\end{aligned} \tag{2.50}$$

We are now ready to proceed and develop the theoretical formula of x-ray TDS.

2.3 Classical theory of x-ray TDS

We will be following the classical treatment in developing the general formula of x-ray TDS (see §2.1). The same result may also be derived via a pure quantum mechanical approach, which may be found in the literatures such as Ref.[13-15].

Consider the general case of a crystal with *n* atoms per unit cell, and suppose it has a total number of *N* unit cells. If we assume the scattering from each atom (without electronic excitations) is always coherent with each other; the total scattering intensity at scattering vector **q** should be given by

$$I = I_e\left\langle\left|\sum_{m=1}^{N}\sum_{s=1}^{n} f_s \exp\left[-i\mathbf{q}\cdot\left(\mathbf{R}_m+\boldsymbol{\tau}_s+\mathbf{u}_{m,s}\right)\right]\right|^2\right\rangle, \tag{2.51}$$

where intensity *I* refers to the photon flux, i.e., the number of photons per unit time and area, f_s is the form factor of the *s*-th atom in a unit cell, $\langle\ldots\rangle$ stands for averaging over time, which is a necessary step as the atoms are moving constantly around their equilibrium positions. I_e is a unit of intensity, it is defined as the intensity measured for the Thomson scattering of a single electron:

$$I_e(\mathbf{q},d) = I_{\text{incident}} \cdot \frac{1}{d^2} \sum_{\alpha'=1,2} \left(\frac{d\sigma}{d\Omega} \right)_{\text{Thomson}}, \tag{2.52}$$

where I_{incident} is the photon flux of the incident x-ray beam, d is the distance from the electron to the observer, α' denotes the polarization of the outgoing photon. If the incident x-ray is linearly polarized, as is the case for common synchrotron radiation, we may write

$$I_e(\mathbf{q},d) = I_{\text{incident}} \frac{r_0^2}{d^2} \left[\sin^2\phi + \cos^2\phi \cos^2(2\theta) \right], \tag{2.53}$$

where 2θ is the scattering angle, ϕ is the angle between the scattering plane (the plane defined by the incident and outgoing x-ray's wavevectors) and the plane defined by the polarization and the direction of the incident beam.

We may rewrite Eq. (2.51) by moving all the time-independent factors outside of the angled bracket:

$$I(\mathbf{q}) = I_e \sum_{m,m'} \sum_{s,s'} f_s f_{s'}^* e^{i\mathbf{q}\cdot(\mathbf{R}_{m'} - \mathbf{R}_m + \boldsymbol{\tau}_{s'} - \boldsymbol{\tau}_s)} \left\langle e^{i\mathbf{q}\cdot(\mathbf{u}_{m',s'} - \mathbf{u}_{m,s})} \right\rangle. \tag{2.54}$$

To evaluate the time average in the equation, we need the following theorem: if A is a linear combination of the position or momentum operators of a harmonic system, then the following equality holds:

$$\left\langle \exp(iA) \right\rangle = \exp\left(-\frac{1}{2} \left\langle A^2 \right\rangle \right). \tag{2.55}$$

Proofs of this relationship may be found in the works by Ott [15], Born and Sarginson [16], or Mermin [17], and will be skipped here. The expression of the total scattered intensity, Eq. (2.54), may now be written as

$$I(\mathbf{q}) = I_e \sum_{m,m'} \sum_{s,s'} f_s f_{s'}^* e^{i\mathbf{q}\cdot(\mathbf{R}_{m,m'} + \boldsymbol{\tau}_{s,s'})} e^{-\frac{1}{2}\left\langle \left[\mathbf{q}\cdot(\mathbf{u}_{m',s'} - \mathbf{u}_{m,s}) \right]^2 \right\rangle} \tag{2.56}$$

The exponent containing the time-average can be further expanded into the following

form:

$$\begin{aligned}
&-\frac{1}{2}\left\langle\left[\mathbf{q}\cdot\left(\mathbf{u}_{m,s}-\mathbf{u}_{m',s'}\right)\right]^2\right\rangle \\
&=-\frac{1}{2}\left\langle\left(\mathbf{q}\cdot\mathbf{u}_{m,s}\right)^2\right\rangle-\frac{1}{2}\left\langle\left(\mathbf{q}\cdot\mathbf{u}_{m',s'}\right)^2\right\rangle+\left\langle\left(\mathbf{q}\cdot\mathbf{u}_{m,s}\right)\left(\mathbf{q}\cdot\mathbf{u}_{m',s'}\right)\right\rangle \\
&\equiv -M_s\left(\mathbf{q}\right)-M_{s'}\left(\mathbf{q}\right)+G_{m,m',s,s'}\left(\mathbf{q}\right),
\end{aligned} \tag{2.57}$$

where $M_s\left(\mathbf{q}\right)$, or sometimes its exponential, $\exp\left[-M_s\left(\mathbf{q}\right)\right]$, is known as the Debye-Waller factor, and is often written without the explicit dependence on **q** in many occasions. Physically, M_s represents the time-averaged deviation of atom *s* from its equilibrium position, projected onto the direction of the scattering vector **q**. In contrast, the last term in Eq. (2.57), $G_{m,m',s,s'}\left(\mathbf{q}\right)$, is related to the correlation between the motion of two atoms (*m*,*s*) and (*m'*,*s'*), and hence carries much richer information about the lattice dynamics of the material.

To establish the mathematical relationship between these quantities and the phonon dispersion, we turn to Eq. (2.47) to write $\mathbf{u}_{m,s}$ as a linear superposition of the lattice normal modes, and arrive at

$$\begin{aligned}
M_s\left(\mathbf{q}\right)&\equiv\frac{1}{2}\left\langle\left(\mathbf{q}\cdot\mathbf{u}_{m,s}\right)^2\right\rangle \\
&=\frac{1}{4\mu_s}\sum_{\mathbf{k},j}\left\langle a_{\mathbf{k},j}^2\right\rangle\left|\mathbf{q}\cdot\mathbf{e}_{\mathbf{k},j,s}\right|^2;
\end{aligned} \tag{2.58}$$

and

$$\begin{aligned}
G_{m,m',s,s'}\left(\mathbf{q}\right)&\equiv\left\langle\left(\mathbf{q}\cdot\mathbf{u}_{m,s}\right)\left(\mathbf{q}\cdot\mathbf{u}_{m',s'}\right)\right\rangle \\
&=\sum_{\mathbf{k},j}\frac{\left\langle a_{\mathbf{k},j}^2\right\rangle}{2\sqrt{\mu_s\mu_{s'}}}\left(\mathbf{q}\cdot\mathbf{e}_{\mathbf{k},j,s}\right)^*\left(\mathbf{q}\cdot\mathbf{e}_{\mathbf{k},j,s'}\right)e^{i\mathbf{k}\cdot\mathbf{R}_{m,m'}}.
\end{aligned} \tag{2.59}$$

Note that Eq. (2.58) would take a simpler form for systems with cubic symmetries, with M_s depending on the magnitude of **q** only:

$$M_s^{(\text{cubic})} = \frac{q^2}{12\mu_s} \sum_{\mathbf{k},j} \left\langle a_{\mathbf{k},j}^2 \right\rangle \left| \mathbf{e}_{\mathbf{k},j,s} \right|^2 . \tag{2.60}$$

The quantity $\left\langle a_{\mathbf{k},j}^2 \right\rangle$ is determined by the Bose-Einstein distribution of the vibrational energy among the normal modes. Substituting Eq. (2.50) into our equations, we arrive at the final expression of the TDS intensity:

$$I(\mathbf{q}) = NI_e \sum_{m=1}^{N} \sum_{s,s'=1}^{n} f_s f_{s'} e^{-i\mathbf{q}\cdot\left(\mathbf{R}_m + \boldsymbol{\tau}_{s,s'}\right)} e^{-M_s - M_{s'}} \exp\left[G_{m,s,s'}(\mathbf{q}) \right], \tag{2.61}$$

with

$$M_s(\mathbf{q}) = \frac{\hbar}{4N\mu_s} \sum_{\mathbf{k},j} \frac{1}{\omega_{\mathbf{k},j}} \coth\left(\frac{\hbar\omega_{\mathbf{k},j}}{2k_B T} \right) \left| \mathbf{q} \cdot \mathbf{e}_{\mathbf{k},j,s} \right|^2, \tag{2.62}$$

$$G_{m,s,s'}(\mathbf{q}) = \frac{\hbar}{2N\sqrt{\mu_s \mu_{s'}}} \sum_{\mathbf{k},j} \frac{1}{\omega_{\mathbf{k},j}} \coth\left(\frac{\hbar\omega_{\mathbf{k},j}}{2k_B T} \right) \left(\mathbf{q} \cdot \mathbf{e}_{\mathbf{k},j,s} \right)^* \left(\mathbf{q} \cdot \mathbf{e}_{\mathbf{k},j,s'} \right) e^{i\mathbf{k}\cdot\mathbf{R}_m} , \tag{2.63}$$

where the summation $\sum_{m,m'=1}^{N}$ in Eq. (2.54) has been replaced with $N\sum_{m=1}^{N}$ in view of the translational symmetry, and the subscript m' is hence dropped from the equation; this change implies first letting $\mathbf{R}_m = 0$, then replacing the indices m' with m.

Had one chosen the non-periodic definition of the dynamical matrix (Eq. (2.45)), the TDS formula would remain the same except for the expression of $G_{m,s,s'}$:

$$G_{m,s,s'}^{(\text{np})}(\mathbf{q}) = \frac{\hbar}{2N\sqrt{\mu_s \mu_{s'}}} \sum_{\mathbf{k},j} \frac{1}{\omega_{\mathbf{k},j}} \coth\left(\frac{\hbar\omega_{\mathbf{k},j}}{2k_B T} \right) \left(\mathbf{q} \cdot \mathbf{e}_{\mathbf{k},j,s}^{(\text{np})} \right)^* \left(\mathbf{q} \cdot \mathbf{e}_{\mathbf{k},j,s'}^{(\text{np})} \right) e^{i\mathbf{k}\cdot\left(\mathbf{R}_m + \boldsymbol{\tau}_{s,s'}\right)} . \tag{2.64}$$

The exponent $G_{m,s,s'}$ is sometimes referred to as the *phonon structure factor*.

2.3.1 First-order and high-order TDS

Although Eqs. (2.61) – (2.63) are simple and elegant, they are not necessarily practical for numerical calculations. With three-dimensional summations in both real and reciprocal space, a sampling grid of 100×100×100 would require 10^{12} times of

evaluations of $G_{m,s,s'}$ at a single scattering vector **q**; for a typical TDS image with 10^4~10^6 different **q** vectors, the computational load is still too demanding for most modern computers. To simplify the problem we may assume $G_{m,s,s'}$ being a small quantity, and expand the exponential $\exp\left(G_{m,s,s'}\right)$ into a power series. The full expression of TDS intensity will hence be expanded accordingly, into a series:

$$I = I_0 + I_1 + I_2 + \ldots \tag{2.65}$$

The leading term of the expansion, or the zeroth-order intensity, has the expression of

$$I_0(\mathbf{q}) = NI_e \sum_{s,s'=1}^{n} \sum_{m=1}^{N} e^{-i\mathbf{q}\cdot\mathbf{R}_m} f_s f_{s'} e^{-i\mathbf{q}\cdot\boldsymbol{\tau}_{s,s'}} e^{-M_s - M_{s'}}. \tag{2.66}$$

To simplify the equation we may use the following identity:

$$\lim_{N\to\infty} \sum_{m=1}^{N} e^{i\mathbf{k}\cdot\mathbf{R}_m} \sim \sum_l \delta(\mathbf{k}-\mathbf{K}_l) \text{ or } N\sum_l \delta_{\mathbf{k},\mathbf{K}_l} \tag{2.67}$$

where $\mathbf{K}_l$ represents the reciprocal lattice vectors, $\delta(\mathbf{k}-\mathbf{K}_l)$ is the Dirac delta function (when **k** is a continuous variable), while $\delta_{\mathbf{k},\mathbf{K}_l}$ is the Kroneker delta (if **k** is discretely defined); depending on the context, both forms of Eq. (2.67) could be useful in our discussions. The zeroth-order term may now be written as

$$I_0(\mathbf{q}) = NI_e \left| \sum_{s=1}^{n} e^{-M_s} f_s e^{-i\mathbf{q}\cdot\boldsymbol{\tau}_s} \right|^2 \sum_l \delta(\mathbf{q}\text{-}\mathbf{K}_l). \tag{2.68}$$

If we ignore the Debye-Waller factors, Eq. (2.68) would represent the Bragg peaks in reciprocal space diffracted by a perfect, non-vibrating lattice, as the sum within the modulus brackets would be exactly the structure factor of one unit cell. With the presence of e^{-M_s} in the equation, however, we see that the Bragg peaks are "modulated", with their intensities always lower than the ideal values (M_s are always positive by definition). This is essentially due to the thermal "smearing" of the atomic charge

densities from their equilibrium distributions. This amount of "deducted" intensity does not simply disappear, but rather goes into the higher order terms of the expansion.

The next term in the expansion of Eq. (2.65) has the expression of

$$\begin{aligned} I_1(\mathbf{q}) &= NI_e \sum_{s,s'=1}^{n} \sum_{m=1}^{N} e^{-i\mathbf{q}\cdot\mathbf{R}_m} f_s f_{s'} e^{-i\mathbf{q}\cdot\boldsymbol{\tau}_{s,s'}} e^{-M_s - M_{s'}} G_{m,s,s'}(\mathbf{q}) \\ &= \frac{\hbar I_e}{2} \sum_{s,s'=1}^{n} \sum_{\mathbf{k},j} \sum_{m=1}^{N} e^{i(\mathbf{k}-\mathbf{q})\cdot\mathbf{R}_m} \left\{ \frac{f_s f_{s'}}{\sqrt{\mu_s \mu_{s'}}} e^{-i\mathbf{q}\cdot\boldsymbol{\tau}_{s,s'}} e^{-M_s - M_{s'}} \right. \\ &\left. \times \left(\mathbf{q}\cdot\mathbf{e}_{\mathbf{k},j,s}\right)^* \left(\mathbf{q}\cdot\mathbf{e}_{\mathbf{k},j,s'}\right) \frac{1}{\omega_{\mathbf{k},j}} \coth\left(\frac{\hbar\omega_{\mathbf{k},j}}{2k_B T}\right) \right\} . \end{aligned} \tag{2.69}$$

Using the discrete form of Eq. (2.67), we may remove both the summations over *m* and over **k**, and arrive at

$$\begin{aligned} I_1(\mathbf{q}) &= \frac{N\hbar I_e}{2} \sum_{j=1}^{3n} \left\{ \frac{1}{\omega_{\mathbf{k},j}} \coth\left(\frac{\hbar\omega_{\mathbf{k},j}}{2k_B T}\right) \left| \sum_{s=1}^{n} \frac{f_s}{\sqrt{\mu_s}} e^{-M_s} \left(\mathbf{q}\cdot\mathbf{e}_{\mathbf{k},j,s}\right)^* e^{i\mathbf{q}\cdot\boldsymbol{\tau}_s} \right|^2 \right\}_{\mathbf{k}=\mathbf{q}-\mathbf{K}_\mathbf{q}} \\ &= \frac{N\hbar I_e}{2} \sum_{j=1}^{3n} \frac{1}{\omega_{\mathbf{q},j}} \coth\left(\frac{\hbar\omega_{\mathbf{q},j}}{2k_B T}\right) \left| \sum_{s=1}^{n} \frac{f_s}{\sqrt{\mu_s}} e^{-M_s} \left(\mathbf{q}\cdot\mathbf{e}_{\mathbf{q},j,s}\right) e^{-i\mathbf{q}\cdot\boldsymbol{\tau}_s} \right|^2 , \end{aligned} \tag{2.70}$$

where $\mathbf{K}_\mathbf{q}$ stands for the nearest reciprocal lattice vector around **q**, as **k** is defined to be within the first Brillouin zone only. Note that Eq. (2.70) holds only for periodic definition of the dynamical matrix. If $\mathbf{D}(\mathbf{q})$ is defined to be non-periodic, we will have

$$\begin{aligned} I_1(\mathbf{q}) &= \frac{N\hbar I_e}{2} \sum_{j=1}^{3n} \frac{1}{\omega_{\mathbf{k},j}} \coth\left(\frac{\hbar\omega_{\mathbf{k},j}}{2k_B T}\right) \left| \sum_{s=1}^{n} \frac{f_s}{\sqrt{\mu_s}} e^{-M_s} \left(\mathbf{q}\cdot\mathbf{e}^{(\mathrm{np})}_{\tilde{\mathbf{q}},j,s}\right) e^{-i\mathbf{K}_\mathbf{q}\cdot\boldsymbol{\tau}_s} \right|^2 \\ &= \frac{N\hbar I_e}{2} \sum_{j=1}^{3n} \frac{1}{\omega_{\mathbf{q},j}} \coth\left(\frac{\hbar\omega_{\mathbf{q},j}}{2k_B T}\right) \left| \sum_{s=1}^{n} \frac{f_s}{\sqrt{\mu_s}} e^{-M_s} \left(\mathbf{q}\cdot\mathbf{e}^{(\mathrm{np})}_{\mathbf{q},j,s}\right) \right|^2 , \end{aligned} \tag{2.71}$$

where $\tilde{\mathbf{q}} \equiv \mathbf{q} - \mathbf{K}_\mathbf{q}$, and the relationship $\mathbf{e}^{(\mathrm{np})}_{\mathbf{q}+\mathbf{k},j,s} = \mathbf{e}^{(\mathrm{np})}_{\mathbf{q},j,s} e^{-i\mathbf{k}\cdot\boldsymbol{\tau}_S}$ was used, which can be easily proved from the definitions.

Unlike $I_0(\mathbf{q})$, which is only nonzero at the Bragg peaks, the first-order term gives rise to an intensity distribution throughout the reciprocal space, and is hence referred to

as the first-order thermal diffuse scattering. A notable property of the first-order TDS is that the intensity at a particular **q** vector depends only on the properties of the phonon modes with the same wavevector **q**. Such a direct correspondence thus forms the basis for TDS being an effective probe of phonon dispersion relations, as first-order TDS is usually the dominant term in the expansion.

The formula for the second-order TDS can be derived, with a bit of patience, to be the following:

$$\begin{aligned} I_2(\mathbf{q}) &= \frac{\hbar^2 I_e}{8} \sum_{\mathbf{k}} \sum_{j,j'} W_{\mathbf{k},j} W_{\mathbf{q}-\mathbf{k},j'} \left| \sum_s \frac{f_s}{\mu_s} e^{-M_s} e^{-i\mathbf{q}\cdot\boldsymbol{\tau}_s} \left(\mathbf{q}\cdot\mathbf{e}_{\mathbf{k},j,s}\right)\left(\mathbf{q}\cdot\mathbf{e}_{\mathbf{q}-\mathbf{k},j',s}\right) \right|^2 \\ \text{or } &= \frac{\hbar^2 N v I_e}{8} \int \frac{d^3\mathbf{k}}{(2\pi)^3} \sum_{j,j'} W_{\mathbf{k},j} W_{\mathbf{q}-\mathbf{k},j'} \left| \sum_s \frac{f_s}{\mu_s} e^{-M_s} e^{-i\mathbf{q}\cdot\boldsymbol{\tau}_s} \left(\mathbf{q}\cdot\mathbf{e}_{\mathbf{k},j,s}\right)\left(\mathbf{q}\cdot\mathbf{e}_{\mathbf{q}-\mathbf{k},j',s}\right) \right|^2, \end{aligned} \tag{2.72}$$

where v represents the volume of a real-space unit cell, $W_{\mathbf{k},j}$ is a short-hand notation of $\frac{1}{\omega_{\mathbf{k},j}} \coth\left(\frac{\hbar\omega_{\mathbf{k},j}}{2k_B T}\right)$, and the integral is over the first Brillouin zone. The same formulae with the non-periodic dynamical matrix definitions are

$$\begin{aligned} I_2(\mathbf{q}) &= \frac{\hbar^2 I_e}{8} \sum_{\mathbf{k}} \sum_{j,j'} W_{\mathbf{k},j} W_{\mathbf{q}-\mathbf{k},j'} \left| \sum_s \frac{f_s}{\mu_s} e^{-M_s} \left(\mathbf{q}\cdot\mathbf{e}^{(\mathrm{np})}_{\mathbf{k},j,s}\right)\left(\mathbf{q}\cdot\mathbf{e}^{(\mathrm{np})}_{\mathbf{q}-\mathbf{k},j',s}\right) \right|^2 \\ \text{or } &= \frac{\hbar^2 N v I_e}{8} \int \frac{d^3\mathbf{k}}{(2\pi)^3} \sum_{j,j'} W_{\mathbf{k},j} W_{\mathbf{q}-\mathbf{k},j'} \left| \sum_s \frac{f_s}{\mu_s} e^{-M_s} \left(\mathbf{q}\cdot\mathbf{e}^{(\mathrm{np})}_{\mathbf{k},j,s}\right)\left(\mathbf{q}\cdot\mathbf{e}^{(\mathrm{np})}_{\mathbf{q}-\mathbf{k},j',s}\right) \right|^2. \end{aligned} \tag{2.73}$$

In the quantum-mechanical picture, the zeroth-, first-, and second-order terms are related to the x-ray photon absorbing or emitting zero, one, and two phonons during the scattering process, respectively, with the total energy and momentum conserved. This can be easily understood through the above expressions of I_0, I_1, and I_2, which, before sums or integrals, involve explicitly the frequencies and eigenvectors of none, one, and two of the phonon modes, respectively.

We could repeat these steps and continue to derive the formulae for the third-order

TDS, forth-order TDS, and so on; however, their expressions would become increasingly complicated and of little practical meaning. This is due to the infinite number of ways that a momentum transfer could be shared between the multiple phonons involved in the scattering process.

We will be referring to the terms with orders of second and above as *high-order TDS* collectively. The issue of how to evaluate the high-order TDS will be discussed in Chapter 3.

List of References

[1] B.E. Warren, *X-ray Diffraction* (Addison-Wesley, Reading, MA, 1968).

[2] J.J. Sakurai, *Advanced Quantum Mechanics* (Addison-Wesley, Reading, MA, 1967), Chapter 2.

[3] V.B. Berestetskii, E.M. Lifshitz, and L.P. Pitaevskii, *Course of Theoretical Physics, vol. 4: Quantum Electrodynamics* (2nd ed., Butterworth-Heinemann, Oxford, 1982), pp.225.

[4] O. Klein and Y. Nishina, *Z. Phys.* **52** (1929) 853; Y. Nishina, *ibid*. **52** (1929) 869.

[5] P.J. Brown, A.G. Fox, E.N.Maslen, M.A. O'Keefe, and B.T.M. Wills, In *International table of crystallography C: Mathematical, Physical and Chemical Tables* (3rd ed.), edited by E. Prince (Published for the International Union of Crystallography by Kluer Adacemic Publishers, Dordrecht /Boston/London, 2004) Chapter 6.1.

[6] J.H. Hubbel, Wm.J. Veigele, E.A. Briggs, R.T. Brown, D.T. Cromer, and R.J. Howerton, *J. Phys. Chem. Ref. Data* **4** (1975) 471; J.H. Hubbel and I. Øverbø, *ibid.* **8** (1979) 69.

[7] J.H. Hubbel, *Radiat. Phys. Chem.* **50** (1997) 113.

[8] H. Ott, *Ann. Phys.* **416** (ser. 5, vol. 23, 1935) 169.

[9] M. Born and J.R. Oppenheimer, *Ann. Phys.* **389** (ser.4, vol. 84, 1927) 457; English translation of the original paper available online at http://www.ulb.ac.be/cpm/people/scientists/bsutclif/bornop.pdf

[10] M. Born and K. Huang, *Dynamical Theory of Crystal Lattices* (Oxford University Press, USA, New York, 1998).

[11] M.P. Marder, *Condensed Matter Physics* (John Wiley, New York, 2000), Chapter 13.

[12] M. Born and T. von Kármán, *Phys. Z.* **13** (1912) 297; *Phys. Z.* **14** (1913) 15; *Phys. Z.* **14** (1913) 65.

[13] S. Sinha, *J. Phys.: Condens. Matter* **13** (2001) 7511.

[14] I. Waller, *Z. Phys.* **51** (1928) 213.
[15] H. Ott, *Ann. Phys.* **416** (ser. 5, vol. 23, 1935) 169.
[16] M. Born and K. Sarginson, *Proc. Roy. Soc.* A **179** (1941) 69.
[17] N.D. Mermin, *J. Math. Phys.* **7** (1966) 1038.

3 Numerical Simulation

First-order, or single-phonon scattering, usually gives the dominant contribution in TDS, and therefore provides a good approximation to the total TDS intensity with a simple formula. However, high-order TDS (multiple-phonon scattering) is by no means always negligible, and in certain occasions, it needs to be carefully accounted for during theoretical calculations. – Two questions are hence important related to high-order TDS: a) under what circumstances would it become significant? b) when it *is* significant, how to evaluate its intensity to a sufficient accuracy?

We will answer these two questions in reversed order: Section 3.1 is dedicated to the numerical solutions for high-order TDS calculation. The all-order algorithm established in §3.1 will then pave the way for a quantitative discussion of question (a) in §3.2 based on specific examples.

3.1 Evaluation of high-order TDS

3.1.1 Second-order TDS

One straightforward approach to estimate high-order TDS is to approximate it with the second-order term only. This is indeed the approach employed in the early TDS studies [1-3]. Due to the limited computational power at the time, further approximation to the lattice dynamics, such as the Debye model [1,2] or isotropic linear-chain-dispersion model [3], was also necessary. Calculations following this approach would yield reasonable estimations, although the accuracy cannot be guaranteed.

With modern computers we may now perform exact calculation of second-order TDS based on Eq. (2.72) or (2.73) without approximations. Basically, for each specific momentum transfer **q**, a numerical integral is performed in the first-Brillouin zone, with the integrand evaluated at every k-point on a dense 3D grid in the reciprocal space. In practice, such a 3D grid typically consists of 20 – 100 points along each dimension and hence has 10^4 – 10^6 points in total. Although simple arithmetic operations of such size should not pose any problem to contemporary PCs, such evaluations may still be too much computationally demanding. The main reason is that the dynamical matrices **D**(**k**) and **D**(**q**–**k**) has to be recalculated and diagonalized at each k-point, and moreover, for **D**(**q**–**k**), it should be repeated for each **q** vector as well. As TDS images taken with an area detector may contain up to 10^6 pixels per exposure with each pixel corresponding to a unique momentum transfer **q**, performing the exact second-order calculation could easily be an overwhelming task in our studies; not to mention that neglecting the terms beyond second-order implies another unknown error in the final result. Nonetheless, exact second-order calculation can be useful when only a small number of **q** vectors are of interest in the problem. In fact, we will be using the exact second-order results as a benchmark test of our all-order algorithm to be introduced below.

3.1.2 The All-Order Algorithm

Our goal is to make accurate evaluations to the high-order intensity. As direct evaluation become virtually impossible beyond the second order, we are forced to abandon the approach of power-series expansion and seek alternative paths starting from the original TDS formula (Eq. (2.61)). In fact, we have not been able to make practical use of the original expression because of two important issues: First, the 3D sums in both real and reciprocal spaces consist of a formidable computational task, and calculations following Eqs.(2.61)-(2.63) are apparently even more complicated than the aforementioned exact

second-order calculations. Second, any practical computation can only be carried out over a finite cluster of the real-space lattice vectors $\mathbf{R}_m$, and it is not obvious whether the calculation can converge at a relatively small cluster size. – We will show, however, that with a carefully designed algorithm, both of these issues can be resolved; and one may evaluate high-order TDS to desirable accuracy with the computational load minimized to an acceptable level.

3.1.2.A. Evaluation of phonon structure factor G

The first issue stated above concerns the complexity of two nested 3D summations in the same formula. Basically, assume that the expression is evaluated over a k-space grid with $N_k = n_k \times n_k \times n_k$ points and a real-space cubic cluster of size $N_R = n_R \times n_R \times n_R$, with n_k and n_R being the number of points along a single dimension, and the number of **q** vectors in the problem is N_q, then we would estimate the total amount of computation to scale as $N_k \times N_R \times N_q = n_k^3 n_R^3 N_q$, which could easily be an exceedingly large number.

To resolve this difficulty let us take a closer look at the expression of the phonon structure factor $G_{s,s'}(\mathbf{q}, \mathbf{R}_m)$ (the dependence on $\mathbf{R}_m$ is now explicitly written), and re-write Eq. (2.63) here:

$$G_{s,s'}(\mathbf{q}, \mathbf{R}_m) = \frac{\hbar}{2N_k \sqrt{\mu_s \mu_{s'}}} \sum_{\mathbf{k},j} \frac{1}{\omega_{\mathbf{k},j}} \coth\left(\frac{\hbar\omega_{\mathbf{k},j}}{2k_B T}\right) \left(\mathbf{q} \cdot \mathbf{e}_{\mathbf{k},j,s}\right)^* \left(\mathbf{q} \cdot \mathbf{e}_{\mathbf{k},j,s'}\right) e^{i\mathbf{k}\cdot\mathbf{R}_m} \quad . \qquad (3.1)$$

Once again, the most time-consuming step during its evaluation should be the calculation and diagonalization of the dynamical matrices **D**(**k**), namely, the step of calculating $\omega_{\mathbf{k},j}$ and $\mathbf{e}_{\mathbf{k},j,s}$ at each k-point. Unlike the calculation of second-order TDS, however, here the dynamical matrices does not have any dependence on **q**. This important fact means

that no matter how many **q** vectors are there in the problem, the values of $\omega_{\mathbf{k},j}$ and $\mathbf{e}_{\mathbf{k},j,s}$ (together with the coth function) need only to be calculated once over a grid of N_k points. As n_k is typically smaller than 100, the amount of memory required to store these values should not be a problem for modern computers either. For tasks with a large number of **q**, this represents a significant reduction to the computational load.

The dependence on **q** and $\mathbf{R}_m$ may be explicitly separated if one write Eq. (3.1) as

$$G_{s,s'}(\mathbf{q},\mathbf{R}_m) = \mathbf{q}^T \cdot \mathbf{\Gamma}_{s,s'}(\mathbf{R}_m) \cdot \mathbf{q}\,, \tag{3.2}$$

where

$$\mathbf{\Gamma}_{s,s'}(\mathbf{R}_m) \equiv \frac{\hbar}{2N_k\sqrt{\mu_s\mu_{s'}}} \sum_{\mathbf{k},j} \frac{1}{\omega_{\mathbf{k},j}} \coth\left(\frac{\hbar\omega_{\mathbf{k},j}}{2k_BT}\right)\left(\mathbf{e}^*_{\mathbf{k},j,s} \otimes \mathbf{e}_{\mathbf{k},j,s'}\right) e^{i\mathbf{k}\cdot\mathbf{R}_m} \tag{3.3}$$

is a matrix function with 3×3 components.

A further step of simplification can be achieved by observing that Eq. (3.1) happens to have the following form:

$$G_{s,s'}(\mathbf{q},\mathbf{R}_m) = \frac{1}{N_k}\sum_{\mathbf{k}=1}^{N_k} g_{s,s';\mathbf{q}}(\mathbf{k}) e^{i\mathbf{k}\cdot\mathbf{R}_m}\,. \tag{3.4}$$

Here

$$g_{s,s';\mathbf{q}}(\mathbf{k}) \equiv \frac{\hbar}{2\sqrt{\mu_s\mu_{s'}}} \frac{1}{\omega_{\mathbf{k},j}} \coth\left(\frac{\hbar\omega_{\mathbf{k},j}}{2k_BT}\right)\left(\mathbf{q}\cdot\mathbf{e}_{\mathbf{k},j,s}\right)^*\left(\mathbf{q}\cdot\mathbf{e}_{\mathbf{k},j,s'}\right). \tag{3.5}$$

It is easy to see that here $g_{s,s';\mathbf{q}}(\mathbf{k})$ is a periodic function in **k** if we have been following the periodic definition of the dynamical matrix. Eq. (3.4) is therefore nothing but a Fourier transformation of the function $g_{s,s';\mathbf{q}}(\mathbf{k})$, and $G_{s,s'}(\mathbf{q},\mathbf{R}_m)$ is simply the Fourier coefficient associated with "frequency" $\mathbf{R}_m$. In view of this specific feature, had we already calculated $g_{s,s';\mathbf{q}}(\mathbf{k})$ on a $n_k \times n_k \times n_k$ grid, a standard fast Fourier

transformation (FFT) procedure would give us the values of $G_{s,s'}(\mathbf{q},\mathbf{R}_m)$ for a same number (n_k^3) of $\mathbf{R}_m$ vectors in real space.

It is well known [4] that the complexity of FFT for a grid of *N* points is $O(N\log N)$, which is compared to $O(N^2)$ for direct calculations. In our case, for each **q** vector, direct evaluation of $G_{s,s'}(\mathbf{q},\mathbf{R}_m)$ one by one for every $\mathbf{R}_m$ needs $N_R \times N_k$ operations; while employing an FFT calculation would allows us to obtain $N_R = N_k$ values of $G_{s,s'}(\mathbf{q},\mathbf{R}_m)$ all in once with only $O(N_k \log N_k)$ complexity. This is hence another significant reduction to the total computing time.

Notice that such a procedure does not have to be repeated for different **q** vectors. In fact, according to Eq. (3.2), instead of evaluating the scalar function $G_{s,s'}(\mathbf{q},\mathbf{R}_m)$ for every single **q**, one may actually choose to evaluate the 9-component matrix function $\mathbf{\Gamma}_{s,s'}(\mathbf{R}_m)$ first, which is a Fourier transformation of the matrix function $\boldsymbol{\gamma}_{s,s'}(\mathbf{k})$ defined as follows

$$\boldsymbol{\gamma}_{s,s'}(\mathbf{k}) \equiv \frac{\hbar}{2\sqrt{\mu_s \mu_{s'}}} \sum_j \frac{1}{\omega_{\mathbf{k},j}} \coth\left(\frac{\hbar\omega_{\mathbf{k},j}}{2k_B T}\right)\left(\mathbf{e}^*_{\mathbf{k},j,s} \otimes \mathbf{e}_{\mathbf{k},j,s'}\right). \tag{3.6}$$

The values of $G_{s,s'}(\mathbf{q},\mathbf{R}_m)$ for any number of **q** vectors are therefore easily derived based on Eq. (3.2) after the 9 FFT operations for each component of $\mathbf{\Gamma}_{s,s'}(\mathbf{R}_m)$ are completed.

Also on a side note, the Debye-Waller factors are calculated during this procedure as well, as we have $M_s(\mathbf{q}) = \frac{1}{2} G_{s,s}(\mathbf{q},0)$ according to Eqs.(2.62) and (2.63).

3.1.2.B. The dependence of $G_{s,s'}$ *on* R_m

With $G_{s,s'}(\mathbf{q},\mathbf{R}_m)$ already evaluated we are left to deal with the following sum in real space:

$$\zeta_{s,s'}^{N_R}(\mathbf{q}) \equiv \sum_{m=1}^{N_R} e^{-i\mathbf{q}\cdot\mathbf{R}_m} \exp\left[G_{m,s,s'}(\mathbf{q},\mathbf{R}_m)\right], \tag{3.7}$$

which is related to the total intensity by

$$I(\mathbf{q}) = N_R I_e \sum_{s,s'=1}^{n} f_s f_{s'} e^{-i\mathbf{q}\cdot\boldsymbol{\tau}_{s,s'}} e^{-M_s - M_{s'}} \zeta_{s,s'}^{N_R}(\mathbf{q}). \tag{3.8}$$

A key issue here is to determine the necessary range of $\mathbf{R}_m$ for the sum $\zeta_{s,s'}^{N_R}(\mathbf{q})$ to converge to its $N_R \to \infty$ limit. A numerical test would have been the most convenient way for such purposes; however, it may not work well at this point, because we do not know the exact answer to the $N_R \to \infty$ limit yet.

To solve the problem it would be helpful to study the behavior of $G_{s,s'}(\mathbf{q},\mathbf{R})$ at large *R* first. As we have previously discussed, $G_{s,s'}(\mathbf{q},\mathbf{R})$ is no more than the Fourier coefficient associated with "frequency" **R** for the periodic function $g_{s,s';\mathbf{q}}(\mathbf{k})$ (see Eq. (3.4)). Mathematically, the high-frequency components may be negligible if $g_{s,s';\mathbf{q}}(\mathbf{k})$ is a smooth, slowly-varying function. In reality, $g_{s,s';\mathbf{q}}(\mathbf{k})$ is indeed so in reciprocal space except for two kinds of exceptions: a) at the k-points where there's an anomaly in the phonon dispersion; b) at the zone center where $\omega_{\mathbf{k},j} = 0$ for the acoustic phonons and $g_{s,s';\mathbf{q}}(\mathbf{k})$ consequently diverges to infinity. They are hence the major sources that contribute to the high-frequency Fourier coefficients, e.g., $G_{s,s'}(\mathbf{q},\mathbf{R})$ at large *R*. Moreover, among these two cases, the latter should almost always give the dominating

contribution due to its divergence. We may therefore write

$$G_{s,s'}(\mathbf{q},\mathbf{R})\big|_{\text{large } R} \approx \frac{1}{N_k} \sum_{\substack{\mathbf{k} \\ (\text{small } k \text{ only})}} g_{s,s';\mathbf{q}}(\mathbf{k}) e^{i\mathbf{k}\cdot\mathbf{R}} . \tag{3.9}$$

Here, the values of $g_{s,s';\mathbf{q}}(\mathbf{k})$ at small *k* are mostly given by the acoustic phonons, which always disperse linearly near the zone-center. Hence for a qualitative discussion, we can use the Debye model as the approximate phonon dispersion, and convert Eq. (3.9) into an integral of **k**:

$$G_{s,s'}(\mathbf{q},\mathbf{R}) \sim k_B T \sum_j \int d^3\mathbf{k} \frac{1}{c^2 k^2} \left(\mathbf{q}\cdot\mathbf{e}_{\mathbf{k},j,s}\right)^* \left(\mathbf{q}\cdot\mathbf{e}_{\mathbf{k},j,s'}\right) e^{i\mathbf{k}\cdot\mathbf{R}} , \tag{3.10}$$

where *c* is the speed of sound, and we have made use of the approximation $\coth(x) \approx \frac{1}{x}$ for small *x*. The expression may be further simplified if we notice that $\mathbf{e}_{\mathbf{k},j,s}$ is a slowly-varying function of **k** and its radial dependence on *k* may be negligible within a small region of k-space. We may then use the spherical coordinates by defining the *z*-axis to be parallel to $\mathbf{R}$, and arrive at

$$\begin{aligned} G_{s,s'}(\mathbf{q},\mathbf{R}) &\sim \sum_j \int A_{s,s',j}(\mathbf{q};\theta,\phi) \sin\theta d\theta d\phi \int_0^{k_D} \frac{\cos(kR\cos\theta)}{c^2 k^2} k^2 dk \\ &\sim \sum_j \int A_{s,s',j}(\mathbf{q};\theta,\phi) \frac{\sin(k_D R\cos\theta)}{R\cos\theta} \sin\theta d\theta d\phi, \end{aligned} \tag{3.11}$$

where θ and ϕ denote the spherical angles within the integral, and $A_{s,s',j}(\mathbf{q};\theta,\phi) \equiv \left(\mathbf{q}\cdot\mathbf{e}_{\mathbf{k},j,s}\right)^* \left(\mathbf{q}\cdot\mathbf{e}_{\mathbf{k},j,s'}\right)$ is a function of the angles only, k_D is the Debye wavevector. We therefore have an important conclusion:

$$G_{s,s'}(\mathbf{q},\mathbf{R}) \propto R^{-1} .$$

In view of this property, we may once again employ the power-series expansion on $\exp\left[G_{s,s'}(\mathbf{q},\mathbf{R}_m)\right]$, and declare that the real-space sum of (3.7) should converge faster for each increasing order of TDS. Namely, once we are sure that the convergence of a certain

order is guaranteed with a certain range of $\mathbf{R}_m$, then calculation for all the higher orders will converge unanimously as well.

3.1.2.C. The real-space sum over $\mathbf{R}_m$

The $O\left(R^{-1}\right)$ behavior of $G_{s,s'}\left(\mathbf{q},\mathbf{R}\right)$ also brings a difficulty to our real-space sum; that is the slow convergence for the lowest orders. At least, by looking at the expression of Eq. (3.7), one might be concerned that the zeroth and first orders would not converge at all. This seems to be a real problem if we examine the zeroth order in detail, as the sum over a simple cubic cluster with would be,

$$\zeta_{s,s'}^{N_R}\left(\mathbf{q}\right)^{(0)}=\sum_{m=1}^{N_R}e^{-i\mathbf{q}\cdot\mathbf{R}_m}=\frac{\sin\left(n_Rq_1a/2\right)}{\sin\left(q_1a/2\right)}\cdot\frac{\sin\left(n_Rq_2a/2\right)}{\sin\left(q_2a/2\right)}\cdot\frac{\sin\left(n_Rq_3a/2\right)}{\sin\left(q_3a/2\right)}\ , \qquad (3.12)$$

where *a* is the lattice constant and $q_{1\ldots3}$ are Cartesian components of **q**. Although it is well known that when $n_R\to\infty$, Eq. (3.12) would be effectively a periodic δ-function; this identity does not really hold for any finite value of n_R at all, as the right hand side of Eq. (3.12) actually fails to converge pointwise in **q** space. In §3.2 we will see numerical examples that summations performed in this manner indeed does not converge for the zeroth, first, and second orders.

To understand this seemingly odd problem, recall that we came with the current form of TDS formula after replacing the double sum $\sum_{m,m'=1}^{N}$ in real space with $N\sum_{m=1}^{N}$, which was based on the translational symmetry of the crystal lattice (see discussion after Eq. (2.63)). This change, however, is no longer valid for a finite-sized atomic cluster, and it's more appropriate for us to write the sum of Eq. (3.7) as

$$\zeta_{s,s'}^{N_R}\left(\mathbf{q}\right)=\frac{1}{N_R}\sum_{m=1}^{N_R}\sum_{m'=1}^{N_R}e^{-i\mathbf{q}\cdot\mathbf{R}_{m,m'}}\exp\left[G_{s,s'}\left(\mathbf{q},\mathbf{R}_{m,m'}\right)\right]. \qquad (3.13)$$

To see how such a change would affect the convergence, one may once again examine the behavior of the zeroth order, which now becomes

$$\begin{aligned}\zeta_{s,s'}^{N_R}(\mathbf{q})^{(0)} &= \frac{1}{N_R}\sum_{m,m'=1}^{N_R} e^{-i\mathbf{q}\cdot\mathbf{R}_{m,m'}} = \frac{1}{N_R}\left|\sum_{m=1}^{N_R} e^{-i\mathbf{q}\cdot\mathbf{R}_m}\right|^2 \\ &= \frac{1}{n_R^3}\frac{\sin^2(n_R q_1 a/2)}{\sin^2(q_1 a/2)}\cdot\frac{\sin^2(n_R q_2 a/2)}{\sin^2(q_2 a/2)}\cdot\frac{\sin^2(n_R q_3 a/2)}{\sin^2(q_3 a/2)},\end{aligned} \tag{3.14}$$

which is clearly rapidly converging to a periodic δ-function at every point in the reciprocal space as n_R increases.

Mathematically, the difference between the two manners of writing the real-space sum is related to the different properties of Dirichlet kernel and Fejér kernel in Fourier analysis; the latter is known to converge much faster than the former by employing an additional loop of sum in its formulation [5].

Examples in §3.2 will show us that the double real-space sum does lead to well-converged results. One might raise another concern that this also introduces an additional loop of 3D sums in real space. However, this problem can be easily bypassed if we notice that for each term in the summation, the only R-vector that matters is $\mathbf{R}_{m,m'} = \mathbf{R}_{m'} - \mathbf{R}_m$; hence we are allowed to effectively write the double summation in the form of a single one as follows:

$$\zeta_{s,s'}^{N_R}(\mathbf{q}) = \frac{1}{N_R}\sum_{\Delta\mathbf{R}} \rho(\Delta\mathbf{R}) e^{-i\mathbf{q}\cdot\Delta\mathbf{R}} \exp\left[G_{s,s'}(\mathbf{q},\Delta\mathbf{R})\right], \tag{3.15}$$

where $\rho(\Delta\mathbf{R})$ is a function that gives the total number of possible $\mathbf{R}_{m,m'}$ vectors for $\mathbf{R}_m$ and $\mathbf{R}_{m'}$ within the same range in real space such that $\mathbf{R}_{m,m'} = \Delta\mathbf{R}$. The specific functional form of $\rho(\Delta\mathbf{R})$ depends on the symmetry of the lattice as well as the shape and size of the real-space cluster; but it should always be easy to figure out based on pure geometrical considerations. Eq. (3.15) therefore represents another fundamental step in our

all-order algorithm. One should keep in mind, however, that by definition the range of possible $\Delta\mathbf{R}$ vectors in Eq. (3.15) is roughly twice the original range of $\mathbf{R}_m$ in each dimension, and N_R is hence $\sim 1/8$ the total number of possible $\Delta\mathbf{R}$ vectors .

With the algorithm introduced above we are essentially equipped to calculate TDS intensities of any particular order. The convergence may not be as good for the first order as it is for the higher orders, yet this does not pose a problem since exact evaluation of first-order TDS is simple (Eqs.(2.70), (2.71)). To compute the total high-order intensity, one may just evaluate the following sum instead of Eq. (3.15):

$$\zeta_{s,s'}^{N_R}(\mathbf{q})_H = \frac{1}{N_R}\sum_{\Delta\mathbf{R}} \rho(\Delta\mathbf{R}) e^{-i\mathbf{q}\cdot\Delta\mathbf{R}} \left\{\exp\left[G_{s,s'}(\mathbf{q},\Delta\mathbf{R})\right] - 1 - G_{s,s'}(\mathbf{q},\Delta\mathbf{R})\right\}. \quad (3.16)$$

3.1.2.D. Summary

In summary, a typical all-order TDS calculation consists of the following steps:

a) Establish a $n_k \times n_k \times n_k$ grid in a k-space unit cell, calculate $\omega_{\mathbf{k},j}$, $\mathbf{e}_{\mathbf{k},j,s}$, and $\coth\left(\hbar\omega_{\mathbf{k},j}/2k_BT\right)$ on each grid point, save their values for the rest of the calculation.

b) Evaluate $\boldsymbol{\gamma}_{s,s'}(\mathbf{k})$ on the n_k^3 grid points according to Eq. (3.6).

c) Do fast Fourier transform for each of the 9 components of $\boldsymbol{\gamma}_{s,s'}(\mathbf{k})$, yielding $\boldsymbol{\Gamma}_{s,s'}(\mathbf{R})$ for $\sim n_k^3$ different $\mathbf{R}$ vectors.

d) Calculate $G_{s,s'}(\mathbf{q},\mathbf{R})$ based on $\boldsymbol{\Gamma}_{s,s'}(\mathbf{R})$ and a given $\mathbf{q}$ vector (Eq. (3.2)).

e) Establish a specific expression for $\rho(\Delta\mathbf{R})$; and compute the real-space sum of Eq. (3.16) (or its modified form for any specific order of TDS).

f) If there are multiple atoms per unit cell, repeat steps (b) to (e) for each pair of *s* and

s'; and calculate high-order TDS based on Eq. (3.8).

g) Do exact first-order calculation after Eq. (2.70) or (2.71);

h) Add up the results of (f) and (g) to get the total TDS intensity.

i) Repeat steps (d) to (h) for each scattering vector **q**.

3.2 Examples and Discussion

3.2.1 Real-space sum and convergence of the all-order algorithm

Let us first demonstrate the difference between the schemes of double and single real-space summations discussed in §3.1.2.C. Fig. 3.1 shows the calculations for the system of Cu crystal (f.c.c.) at 300K with x-ray photon energy of 20 keV; the zeroth-, first-, and second-order intensities were calculated along the (111) direction between the two Bragg peaks of [111] and [222]. The calculations followed our algorithm described in §3.1.2.D with the choice of $n_k =$ 20, 40, 80, and 160; while the real-space sums were performed in the forms of both the single sum (Eq. (3.7)) and the effective double sum (Eq. (3.15)). Results of these calculations are compared with that of the exact calculations of the corresponding orders (first-order according to Eq. (2.70), second-order according to Eq. (2.72); zeroth-order are simply δ-functions); the exact second-order calculation used a dense k-space grid of 200×200×200.

As shown in Figs. 3.1(a), (c), and (e), as the number n_k (and hence the size of the real space cluster) increases, none of the single sum results tends to converge to the correct value given by the exact calculations. On the other hand, when the effective double real-space sum is employed, the calculated zeroth-order intensity (Fig. 3.1(b)) does evolve towards the correct result of simple Bragg peaks (δ-functions) , as discussed in §3.1.2.C, with increasing values of n_k (notice the different vertical scales between

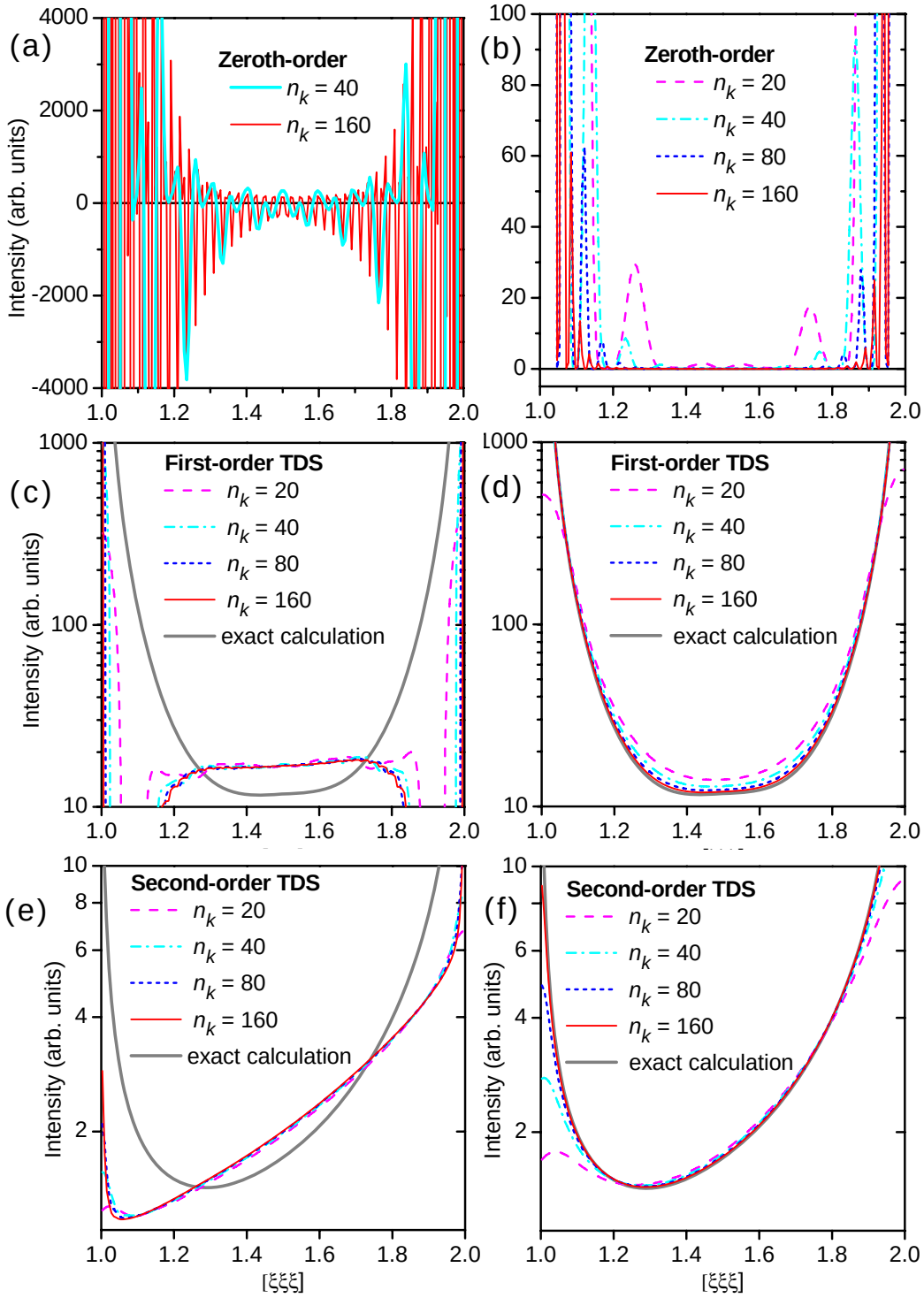

Figure 3.1. Convergence test of the all-order algorithm. The zeroth-order (a,b), first-order (c,d), and second-order (e,f) TDS intensities from a Cu crystal at room temperature calculated along the (111) direction in reciprocal space, between the two Bragg peaks of [111] and [222]. (a,c,e) are computed with single real-space sum while (b,d,f) are computed with the effective double sum in real space (see §3.1.2.C). The exact values of first- and second-order TDS were evaluated according to Eq. (2.70) and Eq. (2.72) respectively. (a,b) are plotted in linear scales, (c-f) in log scales.

figures (a) and (b)). Same convergence is also found in the first-order (Fig. 3.1(d)) and second-order (Fig. 3.1(f)) calculations. Furthermore, comparison between Figs. 3.1(b), (d), and (f) shows that the algorithm indeed gives better convergence for higher orders (again, notice the difference in vertical scales between the plots).

The comparison of the second-order results in Fig. 3.1(f) hence demonstrates the effectiveness and accuracy of using the all-order algorithm to evaluate the high-order TDS intensity. It can be seen that except for regions close to the reciprocal lattice points, high-accuracy (error < 1%) evaluation of high-order TDS can be achieved with the value of n_k between 40 and 80, which would give a typical computing time in the order of 10^{-1} s per **q**-vector on a modern personal computer with a single processor. In contrast, the time cost of the exact second-order calculation, with the same size of k-space grid, is roughly 100 times more than the all-order algorithm.

In practice, choice of n_k is a trade-off between numerical accuracy and calculation speed, and its optimal value should be determined based on the numerical tests described above for each specific system; – typically, a value around 80 is sufficient for many problems.

3.2.2. Importance of high-order in total TDS intensity

With a numerically accurate algorithm we are now equipped to investigate the issue of the relative significance of high-order TDS, or multiple-phonon scattering, within the total scattering process. In fact, despite having the all-order algorithm, it would still be ideal if one could model TDS to sufficient accuracy by using just the first-order formula in real applications. To fulfill this requirement the exponent involved in the expansion, the phonon structure factor *G*, should be a small quantity. Since *G* is defined as $\langle(\mathbf{q}\cdot\mathbf{u})(\mathbf{q}\cdot\mathbf{u}')\rangle$ (Eq. (2.59)), and the magnitude of the atomic displacement **u** is mostly

determined by temperature T for any specific material at thermal equilibrium, the relative importance of high-order TDS should be largely dependent on the magnitude of the two parameters: **q** and T.

As an example, Fig.3.2(a) plots the calculated first-order, high-order, and all-order (total) TDS intensities of Cu at 300 K along an arbitrarily chosen direction of (1, 0.2, 0.02) in reciprocal space. Fig. 3.2(b) presents the computed percentage of high-order intensity relative to the total intensity at two different temperatures, 100 and 300 K. Clearly, high-order effects are more important at larger q and higher T. Assuming that a 3% accuracy is desired, the results show that one should limit q to within $\sim 4\pi/a$ at room temperature, or $\sim 6\pi/a$ at 100 K. Note that T always enters our formulae through the ratio $\hbar\omega/k_B T$, meaning that the temperature limit for a given accuracy should depend on the overall scale of the phonon frequencies within the crystal. A rule of thumb is that

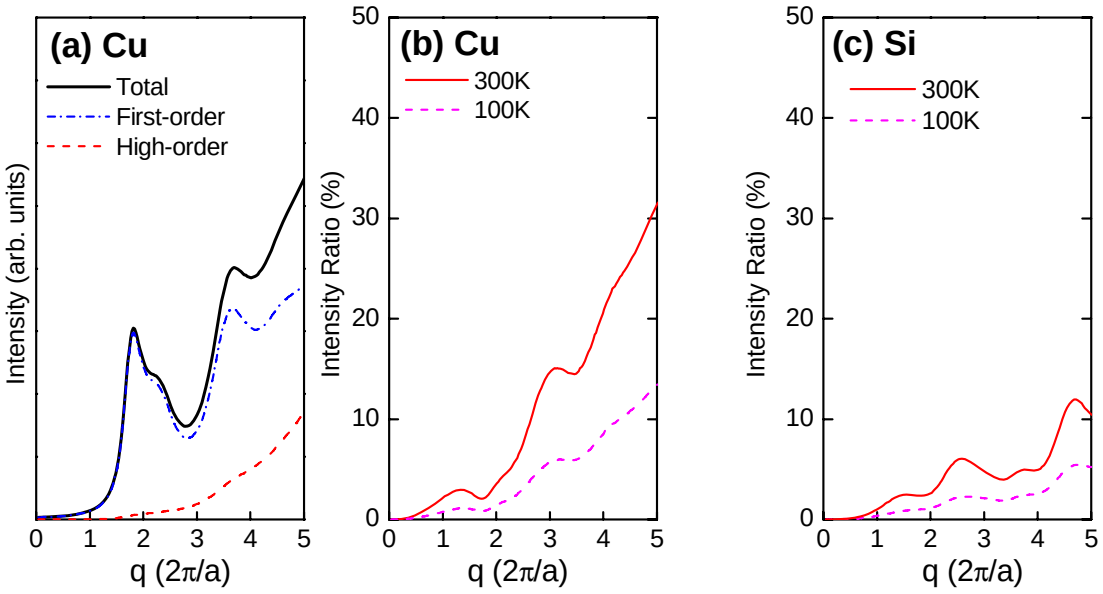

Figure 3.2. (a) Theoretical first-order, high-order, and total TDS intensities of Cu at 300 K for **q** along a random direction of (1.00, 0,20, 0.02) in reciprocal space. (b) Ratio of high-order TDS to total TDS intensities at 300 and 100 K for Cu along the same direction. (c) The same ratio for Si along the same direction at 300 and 100 K.

high-order effects are less important for crystals with a higher Debye temperature. To illustrate this point, we show in Fig. 3.2(c) the computed percentage of high-order TDS intensity relative to the total intensity for Si at the same two temperatures and for the same arbitrarily chosen direction in reciprocal space. There is much less high-order scattering in Si. The Debye temperature of Si is 625 K, which is about twice the value for Cu, 344 K.

3.2.3 Two-dimensional TDS images

Experimental TDS intensity patterns are often recorded with a transmission Laue geometry as two-dimensional images with area detectors. Figure 3.3(a) and (d) shows a calculated example of such images from a Cu crystal at room temperature with its (100) crystal axis parallel to the x-ray beam, displayed in linear and logarithmic scales, respectively. Each pixel in the images corresponds to a unique momentum transfer (or scattering vector **q**) on the Ewald sphere; and the bright areas generally correspond to regions in reciprocal space where phonon frequencies are relatively low, typically near reciprocal lattice points. The contrast in the intensities can be quite large and it is often preferable to present the images in logarithmic scales in order to bring out the rich details of TDS patterns (Fig. 3.3(a)).

Also plotted in Fig. 3.3 are the decomposed intensity patterns of first-order (Fig. 3.3(b), (e)) and high-order TDS (Fig. 3.3(c), (f)). The first-order images are essentially identical to the eye as the all-order ones, indicating its dominance in the total intensity. The weaker high-order intensities are multiplied by a factor of 10 before displayed in the same scale. On top of a gradual increase with the scattering vector q ($q = 0$ at the center of the images), high-order TDS also shows a pattern that appears much like a blurred version of the first-order image.

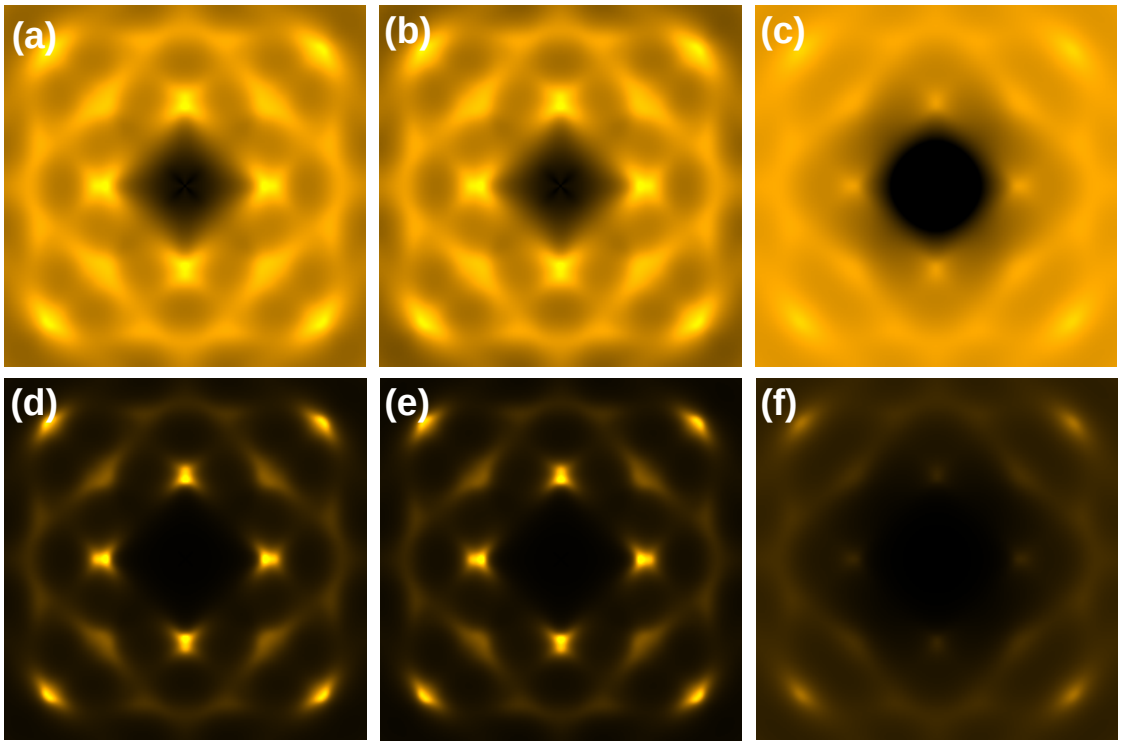

Figure 3.3. Theoretical TDS images of Cu(100) at 300 K assuming an incident x-ray energy of 42 KeV. A logarithmic intensity scale is used for (a) all-order calculation, (b) first-order only, and (c) high-order contribution amplified by a factor of 10. (d)-(f) are the same images presented using a linear scale.

3.2.4 Approximate treatment of high-order TDS

Proper treatment of high-order scattering is a major challenge in the theoretical simulation of TDS. The all-order algorithm introduced in this chapter represents a rigorous solution to this problem. However, it is still a relatively sophisticated procedure; and in certain circumstances, further approximations to high-order TDS may still be necessary.

A simplest practice is to model the high-order intensity patterns as a sum of two parts: a smooth background that increases with q, plus an intensity pattern that is proportional to the first-order one. This is based on the aforementioned observation that high-order patterns appear to resemble that of the first-order, although with much blurred features.

The total TDS intensity may therefore be effectively modeled with just the first-order formula, up to an overall scaling factor plus a smoothly-varying background function. This is the approach used in most of our 2D-image analysis.

Another possible way of quick high-order estimation is replacing the detailed phonon dispersion relation with a simpler model, such as the Debye model, while implementing the all-order algorithm. This would largely reduce the effort for calculating the phonon structure factors *G*, and requires no knowledge of the interatomic force constants within the material. The only input parameter, the Debye temperature of the material, is often easily measurable with other experimental techniques and available in existing literatures. This approach provides a rough estimation of the high-order intensity, although due to the nature of the Debye model it would only generate a smooth, isotropic pattern in the reciprocal space, removing all the detailed structures like those shown in Fig. 3.3(f). We will apply this approximation in our work of momentum-resolved x-ray calorimetry in Chapter 6.

List of References

[1] P. Olmer, *Acta Cryst.* **1** (1948) 57; *Bull. Soc. Franç. Minér.* **71** (1948) 145.
[2] B.E. Warren, *X-ray Diffraction* (Addison-Wesley, Reading, MA, 1968).
[3] C.B. Walker, *Phys. Rev.* **103** (1956) 547.
[4] See, e.g., W.H. Press, B.P. Flannery, S.A. Teukolsky, and W.T. Vetterling, *Numerical Recipes in FORTRAN 77* (2nd ed., Cambridge University Press, Cambridge, 1992).
[5] Y. Katznelson, *An Introduction to Harmonic Analysis* (3rd ed., Cambridge University Press, Cambridge, 2004).

4 TDS as a Method of Phonon Study

4.1 X-ray instruments

4.1.1 Synchrotron light source

Bright x-ray sources are of key importance to TDS measurements due the low crosssection of phonon scattering. A synchrotron light source is therefore an inevitable requirement for efficient and accurate TDS studies.

In a synchrotron source, a group of electrons are first accelerated through several stages to reach a typical energy level of several GeV before they are kept in a horizontal circular orbital under vacuum. Devices called bending magnets are located around the storage ring to steer the electrons around the circle. Upon each flyby of an electron through a bending magnet, centripetal acceleration of the electrons would generate x-ray-wavelength electromagnetic radiations in the forward direction tangent to its path.

On top of the mechanism described above, modern third-generation synchrotron sources use an additional type of component along their storage rings to produce even brighter x-ray radiations. Such instruments are called *insertion devices* or *undulators*. An undulator consists of a periodic, alternating array of dipole magnets along a straight section of the electrons' path. Electrons traveling through this periodic structure are forced to undergo rapid transverse oscillations and emit radiation. Furthermore, it is possible for radiations emitted at each period of oscillation to coherently add up to each other, if they have the specific wavelengths determined by the strength and period of the magnet array. The device can therefore produce x-ray with much higher brilliance and better collimation than the bending magnets.

Radiations from both bending magnets and undulators may be utilized for scientific purposes. X-rays generated from these storage-ring devices are further monochromized and collimated by multiple beamline components along its direction of propagation before reaching a user end station.

Works described in this dissertation are conducted at beamline 33-ID, the Advanced Photon Source (APS). The APS represents one of the three brightest third-generation synchrotron sources in the world. Electrons in its storage ring travels at the energy of 7 GeV through a circle 1104 m in circumference. Beamline 33-ID uses an insertion device and has a typical x-ray flux of 1×10^{13} photons per second.

4.1.2 X-ray detectors

An array of detectors exist for x-ray studies. They are based on distinct fundamental principles and have a broad range of characteristics. Here we briefly describe four types of detectors most commonly used in TDS experiments: ion chambers, scintillation detectors, charge-coupled devices (CCD), and image plates.

A *Gas ionization detector*, or *ion chamber*, usually consist of a closed space filled with air or a specific type of gas, with incident and exit windows for the x-ray beam. Upon passing through this chamber, a small fraction of x-ray photons (depending on the cross section) are absorbed by the gas atoms or molecules, producing electron-ion pairs on the beam's path; and the highly energetic electrons may further induce more ionizations within the gas chamber. Two parallel plates of electrodes, with an applied high voltage, collect the ionized particles. The current is then measured by low-noise electric amplifiers. The electric current therefore serves as a proportional measure of the intensity of the x-ray beam. Due to the low photoionization cross section, however, ion chambers are mainly used to measure the flux of a relatively intense beam instead of detecting single photons.

A *scintillation detector* is a solid-state device that is capable of single-photon

detection. Its detection process includes two stages: first, a layer of scintillating material, usually NaI, absorbs the incident x-ray photon and emits a flash of optical photons; this photon bunch is then collected by a photomultiplier tube which converts the optical signal into a pulse of electric current. The number of photons arrived at the detector is therefore measured by counting of the electric pulses. Counting error could occur, however, when two x-ray photons arrive in almost the same time, in which case they will be counted as a single event. Scintillation detectors are most suitable for measurements of low-flux x-ray signals; the typical upper limit is about 10^6 photons per second.

A *CCD* for hard x-ray detection also requires a conversion of x-ray signals into visible-light photons, which is usually achieved with a phosphor or scintillation screen at the front end of the detector. The generated photons are brought to the CCD chip either with tapperd optical fibers (for large-area detectors) or a high-quality lens (for small-area detectors). Advantages of CCDs include their 2D spatial resolution and short read-out time. However the dynamical range is usually limited; and the signals are subject to intrinsic thermal noises from the semiconductor chip.

An *image plate* is an alternative option to CCD as an area detector. Its main component is a plate coated with phosphor materials whose decay time is in the order of 10^3 seconds. Upon exposure to incident x-rays, the phosphor material is photo-excited to a metastable quantum state. A laser beam is then scanned across the entire area, inducing photoluminescence at each spot which is recorded by optical detectors. Compared to CCD, image plate has excellent dynamical range and much lower intrinsic noise. Yet its long read-out time, roughly 2 minutes per image, poses a significant drawback to its application.

The above four types of detectors are used in complementary to each other in our TDS studies. Ion chambers are mainly for monitoring the incident x-ray beam; scintillation detectors are used as point detectors for line scans in reciprocal space; CCDs are best for quick 2D data collection when time is a concern for the experiment; while an

image plate is preferred for the recording of high-precision TDS images.

4.1.3 Temperature control

It is often necessary to change a sample's temperature during a TDS experiment. In synchrotron x-ray stations this is typically achieved based on a closed-cycle cryostat system named "displex". A displex uses helium gas as its refrigerant. Its major components include a compressor, an expander, and a vacuum shroud. Samples are mounted at the end of the expander's cold stage (also called cold finger), a hollow metal structure made of copper. During each cooling cycle, pressurized helium enters the cold stage, expands in volume and cools down to low temperature. After exchanging heat with the copper wall, the refrigerant gas returns to the compressor to be pressurized again. The cold stage must be contained in vacuum to avoid conduction and convection of the air; while thermal radiation from the vacuum shroud are dealt with a radiation shield surrounding the final section of the cold finger.

In addition to the cooling device, to control the sample temperature one also needs a heating mechanism and a controlling unit. In practice, an electric heating coil is mounted at near end of the displex cold finger, together with a temperature sensor. To reach a prescribed temperature of the sample, the cryostat is kept on all-time, and an externally-connected temperature controller is employed to constantly read the sensor's temperature and adjust the heating current with a PID feedback algorithm.

With a displex, the lowest temperature one can reach is around 7 ~ 10 K, which is sufficient for most phonon studies.

4.2 Probing phonons with TDS

4.2.1 Experimental setup

Depending on sample's characteristics, TDS measurements may be conducted in either

transmission geometry or reflection geometry. The former usually applies to relatively thin samples whose thickness is less than one or several attenuation length; while the latter is a better choice for thick samples. Collection of data may be done in one of the two manners: 2D images or point scans. Taking 2D TDS images with an area detector is a fast and efficient way of TDS data collection; as illustrated in Fig. 4.1, a TDS image represents a 2D cut through the reciprocal space by the Ewald sphere. However, the curved nature of the Ewald sphere means one can not conveniently measure along any specific straight lines in reciprocal space, which, unfortunately, is often desirable in phonon studies. Doing point scans is therefore a useful complementary to 2D-image recording. By using a point detector and a diffractometer, TDS intensities along virtually any specific directions in the sample's reciprocal space can be measured.

To achieve clean experimental data, care should be taken to shield the sample and detector from undesired background intensities. As illustrated in Fig. 4.1, a layer of shielding is typically required when taking 2D images with area detectors to eliminate ambient air scattering originated from upstream. A beamstop made of a thick piece of

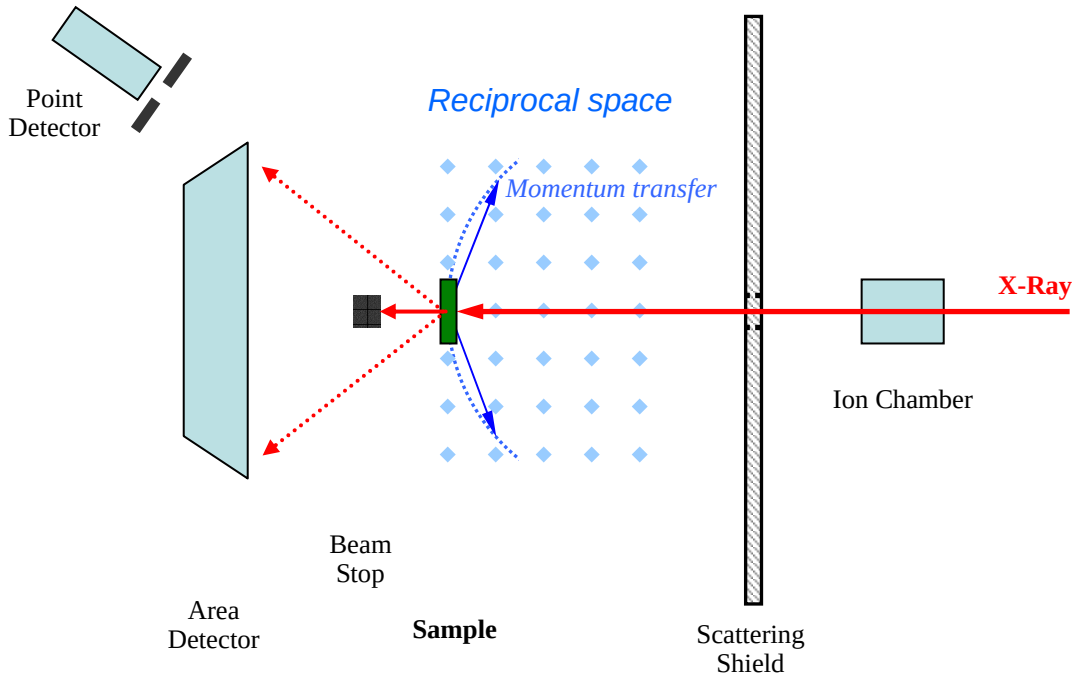

Figure 4.1. Schematic setup of TDS experiment in transmission geometry.

heavy metal is also necessary to prevent the transmitted direct beam from reaching the detector or giving rise to additional air scattering. Besides, an ion-chamber detector is usually installed upstream to the sample to monitor the intensity variation of the incident beam.

4.2.2 Data processing

Extracting phonon information from experimental data is a reverse process of the numerical simulation described in Chapter 3. Although there are no analytical expressions of phonon frequencies in terms of TDS intensities, one may solve for the answer through a numerical fitting procedure. More specifically, one first adopt a Born-von Kármán model with force constants up to a number of nearest neighbors to describe the phonon dispersion relations of the material. Staring with some initial guess of the force constants, phonon eigenvalues and eigenvectors can be calculated to generate a theoretical TDS pattern. The computed results are then compared with the experimental data. Through an iterative process the force constants are constantly adjusted until a minimum difference between theory and experiment is reached. Aside from the force constants, other quantities may also be inserted as fitting parameters, such as the Euler angles of the sample's orientation, the distance between sample to detector, the overall intensity scale factor, and so on. It is also necessary to properly model the background intensities, which may consist of Compton scattering, residue ambient scattering, and detector noises, etc. In view of their nature, these backgrounds can usually be modeled with a smooth function of the scattering angle.

4.2.3 Previous examples

The first modern-era TDS phonon study was performed on silicon crystals in 1999 [1] by the previous student M. Holt in our group. Using transmission geometry, 2D TDS images from both (111) and (001) oriented crystals were recorded with an image plate at room

temperature. A force-constant model analysis including sixth nearest atomic neighbors was conducted via least-squares fitting; and the result was in excellent agreement with the existing neutron scattering data. A similar experiment on Nb was later performed [2] with TDS images recorded in three different crystal orientations. The deduced phonon dispersion relations show a reasonable agreement with neutron data. The discrepancies were partly attributed to the limitation of the lattice dynamics model used in the analysis, which will be discussed further in chapter 6.

An important area of application for TDS is phase transitions. The efficiency of the method makes it feasible to take data at closely spaced intervals of temperature, pressure, or applied field. Holt *et al.* performed such studies of $TiSe_2$ [3] and $SrTiO_3$ [4]. $TiSe_2$ has a charge-density wave transition at ~200 K, which results in a commensurate ($2\times2\times2$) superlattice at lower temperatures. The transition involves a softening of the L_1^- phonon mode at the zone boundary. The TDS experiment took line scans in reciprocal space along a particular direction across the *L* point with a point detector. An increase of the TDS intensities near the *L* point was observed as the sample temperature was lowered toward the transition. Eventually a Bragg peak emerged at the transition temperature and became more intense as the temperature was reduced further. Quantitative analysis was performed by fitting the observed TDS lineshapes using a force constant model, with only one of the force constants, which is associated with the softening of the L_1^- mode, allowed to vary with temperature. The resulting dispersion curves revealed a power law behavior in the softening of the L_1^- mode in agreement with the prediction of a Landau mean-field theory. The investigation on the soft mode on $SrTiO_3$ [4] followed similar procedures.

The methodology described above was implemented in our studies on structural phase transitions in plutonium, which will be the topic of the next chapter.

List of References

[1] M. Holt, Z. Wu, H. Hong, P. Zschack, P. Jemian, J. Tischler, H. Chen, and T.-C. Chiang, *Phys. Rev. Lett.* **83** (1999) 3317;
[2] M. Holt, P. Czoschke, H. Hong, P. Zschack, H. K. Birnbaum and T.-C. Chiang, *Phys. Rev. B* **66** (2002) 064303.
[3] M. Holt, P. Zschack, H. Hong, M.Y. Chou, and T.-C. Chiang, *Phys. Rev. Lett.* **86** (2001) 3799.
[4] M. Holt, M. Sutton, P. Zschack, H. Hong, and T.-C Chiang, *Phys. Rev. Lett.* **98** (2007) 065501.

5 Phonons in Plutonium

5.1 Introduction

Plutonium is a curious element in the periodic table. Aside from its famous application as a nuclear material, it has also been a focus of great scientific interest due to its surprisingly complex physical and chemical properties. Most notably, metallic plutonium has as many as six different allotropies at ambient pressure below the melting point, with significant variations in their structure, volume, ductility, etc. A number of unusual features have also been discovered in its melting, thermal expansion, electric conductivity, magnetic susceptibility, specific heat, and so on [1]. Arguably the most complex metallic element, plutonium is described as a "physicist's dream and engineer's nightmare".

Much of plutonium's rich phenomena are yet to be explained, but they are believed to be closely related to the 5f electrons. In fact, a fundamental trend in the actinides metals is that the 5f electrons switches gradually from bonding in the lighter actinides ($_{90}$Th to $_{93}$Np) to localized in the heavier members ($_{95}$Am, $_{96}$Cm, and beyond), as has been confirmed by local magnetic moments measurements [1]. Pu, however, is located right at the middle of this transition. Studies show that the 5f electrons in Pu do not exhibit a particularly preferred behavior, and their degrees of localization can be highly sensitive to subtle changes in the external parameters such as temperature, pressure, or doping; this is thus connected to many of plutonium's peculiarities [1,2].

Among all the solid phases of Pu, the fcc δ-phase is particularly important in practice due to its engineering-friendly properties. Although the δ-phase of pure plutonium is only stable at temperatures higher than room temperature, it has been found that its stability can

be retained at low temperatures by doping with other metals such as americium, gallium or aluminum. In fact, so far most experimental studies on δ-Pu were carried out with alloy-stabilized samples [1,2].

5.1.1 Phonon dispersions in δ-plutonium

Despite being a fundamental physical property, the phonon dispersion relations of plutonium have long eluded people's grasp due largely to the unavailability of single crystal samples big enough in size for neutron scattering experiments. Mapping of δ-Pu's phonon dispersion relation was finally achieved at the beginning of this century, with high-resolution inelastic x-ray scattering (IXS) [3]. Instead of a single crystal, a large-grain, polycrystalline sample was used, with the incident x-ray beam focused down to micrometer size to ensure single-grain measurements. The experiment revealed dispersion curves along three major high-symmetry directions of δ-Pu in reciprocal space, as shown in

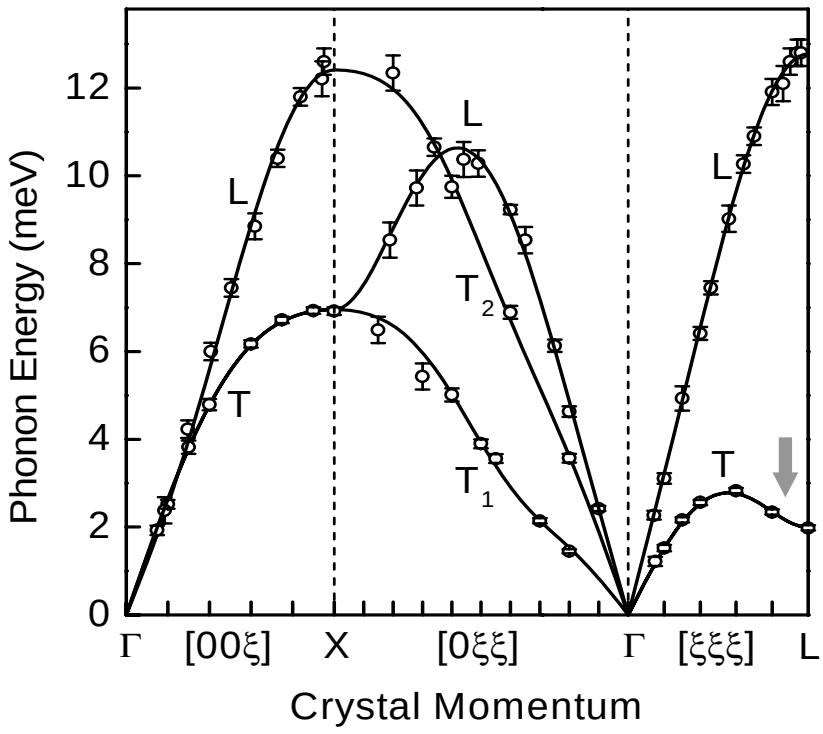

Figure 5.1. Phonon dispersion curves of δ-Pu (0.6 wt.% Ga) at room temperature. Measured by inelastic x-xay scattering (Ref. [3]). Arrow indicates the T[111] branch.

Fig. 5.1.

Several very interesting features in the dispersion curves were revealed, including the unusually close transverse (T) and longitudinal (L) speeds of sound in the [001] direction, and a Kohn-anomaly-like kink in the [011] direction. Most prominently, the T[111] phonon branch exhibits a profound dip near the *L*-point at the zone boundary. This soft phonon mode implies a weak restoring force for the (111) atomic planes to slide anti-parallel to their neighbors, and was therefore suspected to be related to the δ–α' structural phase transition of this material that might take place through a lattice-shearing mechanism.

5.1.2 The δ–α' transition in Pu-Ga

Depending on the gallium content, stability of the δ-phase Pu-Ga may be retained either down to zero Kelvin (highly-doped) or to some point below room temperature (low-doped) [1,2]. The sample in the aforementioned IXS experiment contained 2.0% gallium in number of atoms, and would actually transform into a low-temperature α'-phase below ~170K. Much similar to the α-phase of pure Pu, the α'-phase of Pu-Ga has a monoclinic lattice with 16 atoms per unit cell, with the only difference being that the latter is actually an oversaturated solid solution of gallium with a slightly different lattice constant [1,2].

The δ–α' transition has been a subject of much attention. Despite its apparent complexity and lack of symmetry, the monoclinic α'-phase may essentially be viewed as a distorted hcp structure, with the same "A-B-A-B" sequence of stacking of atomic planes. Hence it has long been speculated that the δ–α'transition may take place through a displacive, lattice-shearing mechanism by re-shuffling of the fcc (111) atomic planes [1]. This hypothesis was later confirmed by experimental studies with transmission electron microscopy (TEM), which established a lattice correspondence between the two phases as $(111)_{\delta} \| (020)_{\alpha'}$ and $[-110]_{\delta} \| [100]_{\alpha'}$ [5].

The observation of a profoundly soft T[111] phonon mode at the zone boundary

therefore seem to be closely related to this transition. A particularly interesting issue, then, is how this phonon branch would evolve when temperature is lowered towards the transition, and a TDS experiment was designed to investigate this problem.

5.2 Experiment

We studied a Pu-Ga sample with the same composition as the one in the IXS experiment [3], namely, 2.0% Ga in atomic number or 0.6% in weight. The sample was carefully prepared by our collaborators at the Lawrence Livermore National Laboratory. The alloy was first compressed and annealed in vacuum for a number of days to promote the growth of large single crystal grains. The resulting polycrystalline sample was machined down to 2.8 mm in diameter and ~12 μm in thickness, and was immediately coated with a thin layer of polyimide. The size of the single crystal grains was in the order of 50 μm according to optical micrographic images. The small thickness of the sample is necessary for a transmission TDS experiment since plutonium is a dense material and has short attenuation lengths for x-rays. The polyimide coating protects the sample from oxidation, as plutonium is also highly reactive and would burn spontaneously in air.

The prepared sample was then sealed in an aluminum chamber for safety reasons. The assembly was mounted on the cold finger of a closed-cycle helium cryostat (displex). Immediately outside the wall of the aluminum chamber, at the position of the outgoing x-ray beam was a small, millimeter-thick lead disc serving as a beam stop to block the transmitted direct beam. Enclosing the sample chamber was specially designed vacuum shroud with two kapton windows on opposite sides, with the outgoing window providing ~60 degrees of angular span for scattered x-rays. The sample temperature was controlled by a built-in heater, a silicon diode temperature sensor, and a feedback system.

The x-ray measurements were performed at beamline 33-ID, Advanced Photon Source, Argonne National Laboratory. The beam energy was set at 18.0 keV, just below the Pu L_3 edge at 18.056 keV, but also sufficiently high for substantial x-ray transmission though the

Pu sample and the aluminum chamber walls. A pair of Kirkpatrick-Baez mirrors was employed to focus the beam to the size of 8 μm × 8 μm in FWHM.

A crucial step during the experiment was to identify the positions of the "good" single crystal grains, namely, the sample positions for the transmitting x-ray beam to shine through the least amount of impurities or grain-boundaries (preferably none). This was done by doing 2D area scans on the sample with prescribed step sizes. Quick TDS images (~1 sec per exposure) were taken at each step during the scan with a CCD detector. Noise level and overall symmetry of the TDS images are easily-identifiable features to the eyes, and were used to evaluate the sample's quality at each different spot across the area.

The 2D survey was carried out in three stages: a coarse scan with 40 μm in step size, yielding several candidate areas on the sample, followed by fine scans in each selected region with 15 μm steps, and eventually some ultra-fine scans with 5 μm steps to carefully map the boundaries of each grain. – Two major single crystal grains, with surface normal parallel to the (111) and (011) crystallographic directions, respectively, were eventually selected for data collection.

Transmission TDS images from the sample were recorded at the two selected grains with a MAR345 image plate detector. Starting from ambient temperature of 307K, data was collected at sample temperatures of 280K, 260K, 240K, 220K and 200K, respectively. A 30 K safety margin from the δ–α' transition at ~170 K was maintained to avoid irreversible domain structure changes at the transition. After each temperature change, there would be a non-negligible shrink, in the order of 10^{-1} mm, in the length of the cold finger, and hence in the sample's vertical position. To ensure that the beam is always probing the same spot on the sample, an additional 2D area scan with 5 μm ultrafine steps was conducted after each temperature change as a re-calibration of the position of the individual grain. After this procedure, TDS images were collected through multiple exposures with typical exposure time of 1~2 minutes. The total exposure time at each temperature rages from 50 to 200 minutes.

5.3 Data and analysis

Figure 5.2 (a)-(c) shows the integrated TDS images from the (111) grain at temperatures of 307K, 260K, and 200K, respectively, and those from the (011) grain are shown in Figs. 5.2 (g)-(i). All images were presented using a logarithmic intensity scale. The dark circle at the center of each image is the shadow of the lead beam stop. One can see that despite our extensive efforts to locate the "best" single crystal spots on the sample, there are still some evident Debye rings present in the recorded TDS images. These arise from impurity phases in the sample (mainly microcrystalline δ-Pu-Ga and PuO) and chamber components. A software algorithm was employed to mask out these Debye rings during data analysis.

The analysis employed a fourth-nearest-neighbor Born-von Kármán (BvK) force constant model to generate theoretical TDS images in both (111) and (011) orientations for a fit to the data. The BvK force constants, however, were not directly used as fitting parameters. Rather, the fitting procedure was designed to be sensitive exclusively to the T[111] branch only, and is achieved as follows. The primary fitting parameters are the planar force constants (PFCs) responsible for (111) atomic layer sliding, with PFCs up to the second nearest-neighbors of atomic layers included. For each updated set of these planar force constants, a new set of BvK force constants was generated to describe the full phonon dispersion curves consist of the new, updated T[111] branch and all the other branches fixed to their original positions. Theoretical TDS images were then computed based on this new set of BvK force constants and compared to the experimental data during each step of iteration before the final convergence is reached.

The fitted TDS images are shown in Figs. 5.2(d)-(f) and (j)-(l). Visually the agreement is excellent except for the areas covered by the Debye rings and the beam stop, where the data were excluded from the fitting.

Figure 5.3(a) shows the dispersion curves for the T[111] branch from the fits at various temperatures between 307 K and 200 K. Also included are data from prior IXS results

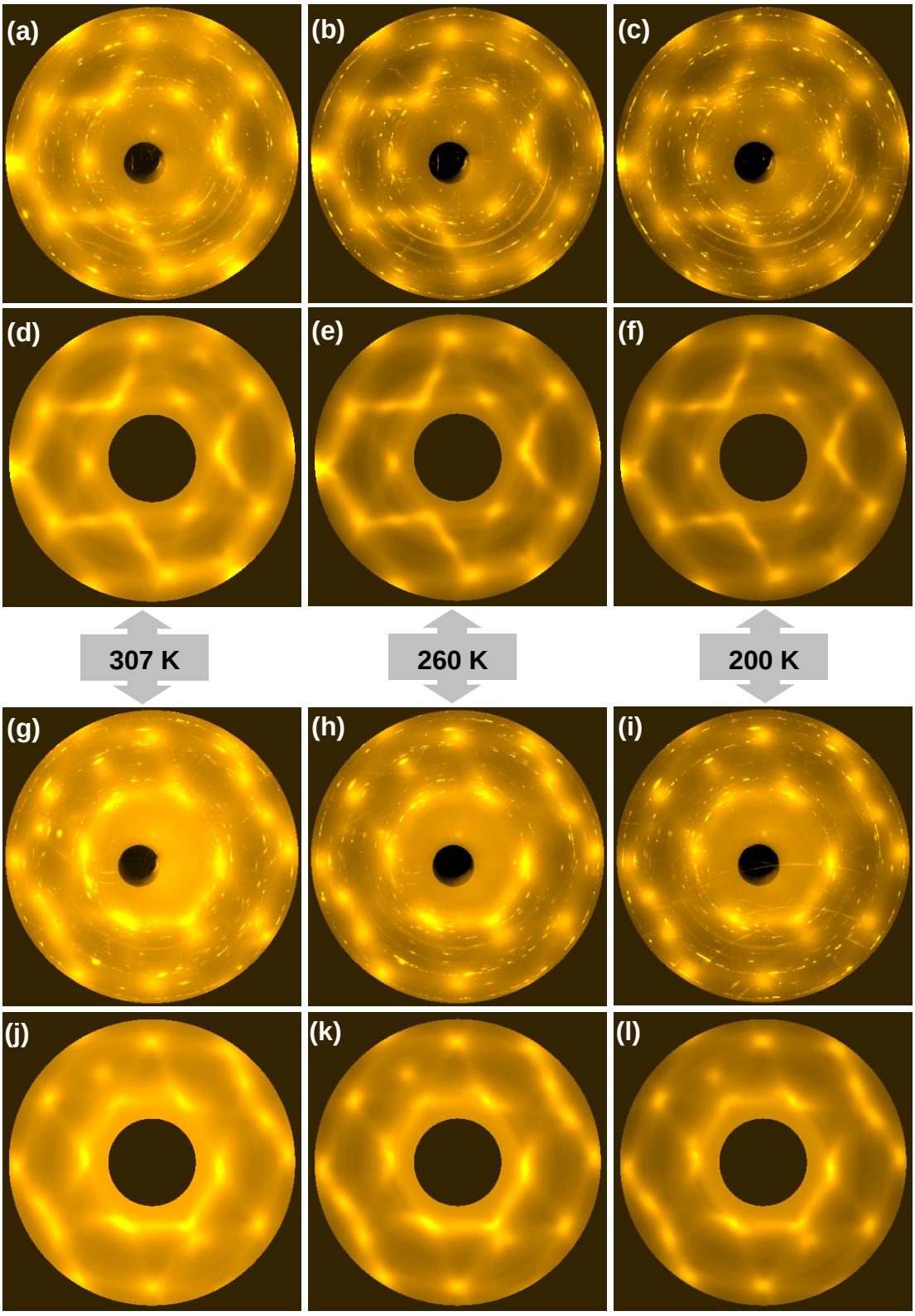

Figure 5.2. X-ray TDS images of δ-Pu-Ga at 307K, 260K, and 200K. (a)-(c) are the experimental images of the (111) grain; (d)-(f) are their corresponding theoretical fits; (g)-(l) are the same set of experimetal and fit images of the (011) grain.

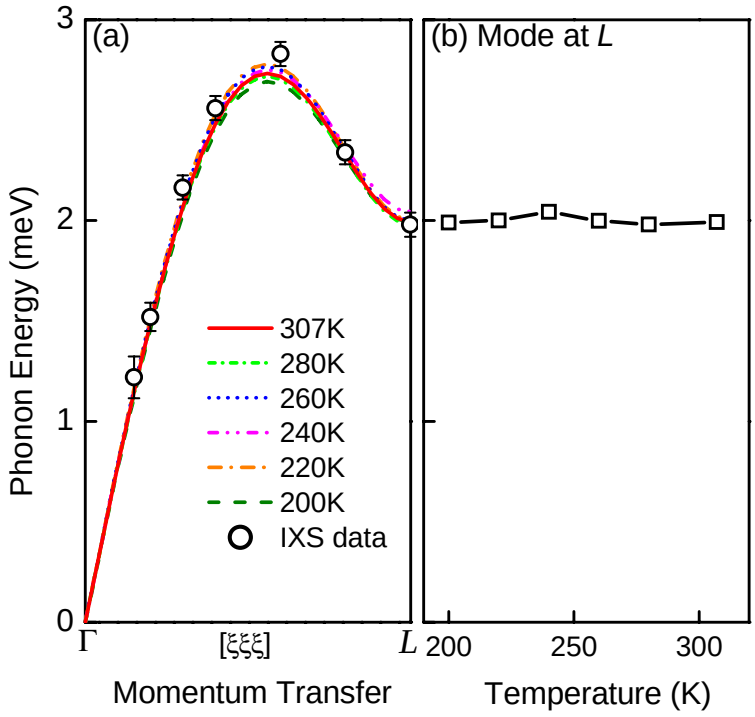

Figure 5.3. (a) Derived dispersion curve of the T[111] phonon branch of δ-Pu-Ga at different temperatures; (b) temperature dependence of the phonon energy at the *L* point

obtained at room temperature [3,4]. Contrary to the previous conjectures, there is little or no temperature dependence, which can also be seen from Fig. 5.3(b), the frequency of the transverse mode at the *L* point as a function of temperature. Hence, the restoring force against (111) atomic layer sliding does not weaken toward the transition.

5.4 Discussion

Comparison may be drawn between δ-Pu-Ga and two other transition metals: γ-Ce and β-La. In fact, these three systems bear many similarities to each other: They all have fcc crystal structure; their overall phonon dispersion curves look strikingly similar, including the dip in the T[111] branch near the *L*-point, aside from an overall energy scale [6,7]; moreover, γ-Ce and β-La both transform into a low-temperature phase (dhcp) upon cooling,

through a similar lattice-shearing mechanism as the δ–α' transition in Pu-Ga. Unlike δ-Pu-Ga, however, both γ-Ce and β-La show softening in the T[111] phonon branch when the temperature is lowered towards the transitions, although the softening is only partial and the zone-boundary phonon frequencies do not really become zero [6,7]. Thus compared to Ce and La, the behavior of Pu-Ga seems to belong to a different type of displacive structural transition.

Phenomenologically, the Landau free energy of a system near a displacive transition may be expressed in terms of an expansion:

$$F = \alpha\xi^2 + \beta\xi^4 + \gamma\xi^6 + \ldots,$$

where ξ is the order parameter and α, β and γ are the expansion coefficients. The order parameter can be regarded as the generalized coordinate associated with the soft phonon mode, whose frequency is determined by the curvature of $F(\xi)$ at $\xi = 0$, i.e., coefficient α. For second-order transitions, γ may be ignored as β usually assumes a constant positive value, while the value of α depends strongly on temperature, and switches its sign during the transition (see Figs. 5.4(a) and (b)). For first-order transitions, β is negative, and γ must be positive for the system to be stable. The resulting $F(\xi)$ curve has two minima, one at $\xi = 0$ and the other at $\xi > 0$ (Figs. 5.4(c) and (e)). Similar to the second-order transitions, the coefficient α usually assumes a strong temperature dependence as well. – As illustrated in Fig. 5.4(c) (labelled type-A), the transition takes place when T is lowered to below T_C, which is the temperature for the secondary minimum at $\xi > 0$ to move below the primary one at $\xi = 0$. Decrease of α with decreasing temperature toward T_C therefore gives rise to a partial softening of the phonon mode (Fig. 5.4(d)), and the behaviors of γ-Ce and β-La fits this description.

For the δ–α' transition of Pu-Ga, however, the curvature at the primary minimum at $\xi = 0$ does not appear to have a measurable temperature dependence as no phonon

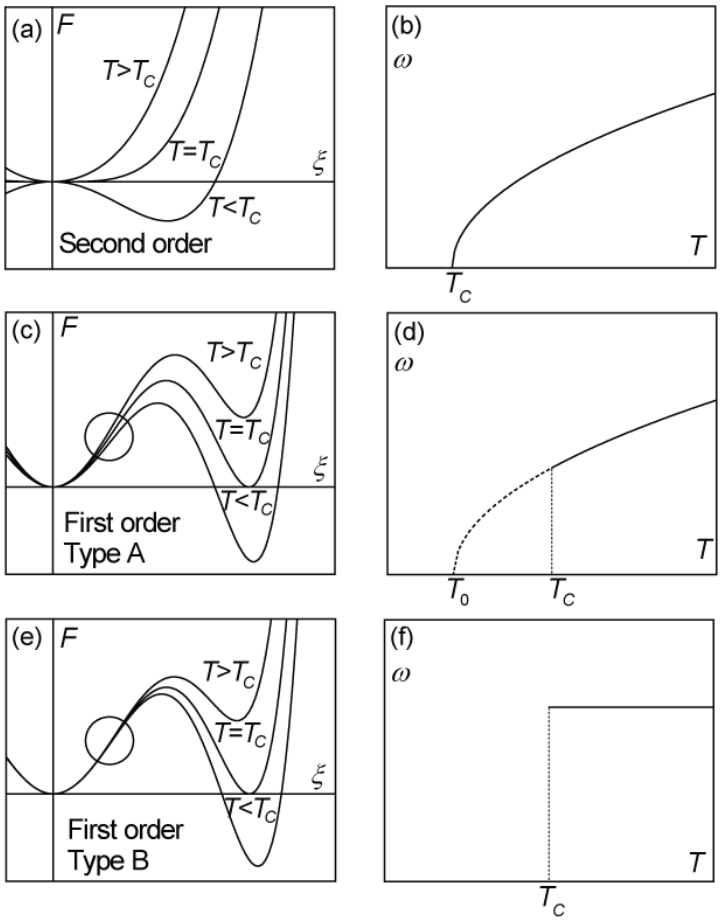

Figure 5.4. (a,c,e) Schematic diagrams of Landau free energy as a function of the order parameter for different types of displacive structural transitions. (b,d,f) The temperature-dependence of the associated phonon frequency.

softening was observed. Thus, α must remain nearly constant. There are two possible explanations. One is that although the coefficient α is temperature-dependent, its variation over the temperature range is just too small to give rise to a noticeable effect on the soft mode frequency; an implication is that the difference in free energy between the primary and secondary minima remains rather small over the temperature range of interest. Another explanation is that this transition is of a different type – type B. Instead of α, it is the next coefficient β that bears the major temperature dependence in the free energy. As illustrated in Fig. 5.4(e), increase in the absolute value of β would also lead to a lowering of the

secondary minimum at $\xi > 0$, therefore driving the transition, but the harmonic frequency for vibrations around $\xi = 0$ remains fixed (Fig. 5.4(f)). The present results on Pu-Ga can be explained either way, and more work is needed to distinguish the two possibilities.

In any case, the unusual behaviour of Pu-Ga is likely a result of the complex properties of Pu's 5f electrons. Further theoretical studies using advanced computational tools would be needed for a detailed understanding of the relationship between electronic effects and soft phonon modes.

List of References

[1] *Los Alamos Science*, No. **26**, Vol. 1 & 2, edited by N.G. Cooper (2000).
[2] S. S. Hecker, D. R. Harbur and T. G. Zocco, *Prog. Mater. Sci.* **49** (2004) 429.
[3] J. Wong, M. Krisch, D. L. Farber, F. Occelli, A. J. Schwartz, T.-C. Chiang, M. Wall, C. Boro and R. Xu, *Science* **301** (2003) 1078; G. Lander, *Science*, **301** (2003) 1057.
[4] J. Wong, M. Krisch, D. L. Farber, F. Occelli, R. Xu, T.-C. Chiang, D. Clatterbuck, A. J. Schwartz, M. Wall and C. Boro, *Phys. Rev. B* **72** (2005) 064115.
[5] T.G. Zocco, M. F. Stevens, P. H. Alder, R. T. Sheldon and G. B. Olson, *Acta Metall. Mater.* **38** (1990) 2775.
[8] C, Stassis, C.-K. Loong and O. D. McMasters, Phys. Rev. B **25** 6485 (1982).
[9] C. Stassis, C.-K. Loong and J. Zarestky, Phys. Rev. B **26** 5426 (1982).

6 Momentum-resolved x-ray calorimetry

6.1 Motivation

Investigations on Pu once again demonstrated the effectiveness of TDS as a technique of phonon study. Yet there are still limitations to its application due to some factors in its implementation. First and most important of all, description of a material's phonon dispersion relation was made with a force-constant model. The accuracy of the result is therefore systematically limited by the model's quality as an approximation to the dynamics of the lattice. In the case of niobium, for instance, it has been known that even with the eighth-nearest-neighbor included, a force-constant model cannot give a sufficiently accurate description of the measured phonon dispersion curves [1], and the results of TDS study [2] showed discernable deviations from the neutron scattering data. Force constant models usually has problem reproducing the abrupt anomalies in the dispersion curves; such anomalies are therefore undetectable to our TDS method.

Another issue of the previous TDS works is the relatively complicated data analysis procedure. A nonlinear least-squares fitting with dozens of parameters may easily get trapped at local minima and yield fake answers to a problem. Usually a fairly many number of numerical runs with different initial guess to the fitting parameters are necessary to identify a best result.

It would therefore be highly desired if TDS can be utilized with an alternative approach so that the phonon information it contains can be derived without the need of a model, and with some easier numerical procedures. In next section we will introduce a

feasible solution to this problem.

6.2 Theory

The approach followed in the previous works was based on TDS patterns, i.e., scattered intensity as a function of momentum transfers in reciprocal space. In contrast, we propose a new procedure that examines the functional dependence of TDS on temperature. To see how the temperature-dependence of intensities is related to the phonon dispersions, one may write down the first-order TDS formula (Eq. (2.70)):

$$I_1(\mathbf{q}) = \frac{N\hbar I_e}{2}\sum_{j=1}^{3n}\frac{1}{\omega_{\mathbf{q},j}}\coth\left(\frac{\hbar\omega_{\mathbf{q},j}}{2k_BT}\right)\left|\sum_{s=1}^{n}\frac{f_s}{\sqrt{\mu_s}}e^{-M_s}\left(\mathbf{q}\cdot\mathbf{e}_{\mathbf{q},j,s}\right)e^{-i\mathbf{q}\cdot\boldsymbol{\tau}_s}\right|^2 .$$

Apparently, the functional dependence of $I_1(\mathbf{q})$ on temperature T is carried solely by the hyperbolic cotangent function, and is directly modulated by the phonon frequencies $\omega_{\mathbf{q},j}$. Therefore, once the dependence of TDS intensity on temperature is measured, one may straightforwardly solve for the phonon frequencies as unknowns in the equation.

The problem can be further simplified by using polarization selections. That is, if the scattering vector **q** is selected to be along certain high-symmetry directions in reciprocal space, presence of the $\left(\mathbf{q}\cdot\mathbf{e}_{\mathbf{q},j,s}\right)$ factor would yield zero scattering contributions for those phonon branches whose polarizations are perpendicular to **q**; effectively reducing the number of unknown frequencies in the equation. For the simple case of monatomic crystals, it is possible to have just one phonon mode contributing to the total intensity.

The above arguments are based on first-order TDS formula only; thus for this method to work it is important that high-order scattering can be properly accounted for during the analysis. Accurate evaluation according to our all-order algorithm, however, is not possible as we assume no detailed knowledge on the lattice dynamics of the sample. Nonetheless, if we limit our study to relatively low temperatures and small magnitude of **q** vectors, the percentage of high-order in total TDS intensity can be minimized, and a

rough approximation could suffice our analysis. We will be using the Debye model in estimating the high-order scattering during our test study on copper.

6.3 Example of Cu

6.3.1 Experiment

The new approach was first tested in the model system of copper, which has a simple fcc crystal structure with one atom per unit cell. The experiment was again performed at sector 33-ID of the Advanced Photon Source. A Cu single crystal with (110) surface normal was prepared by mechanical polishing to a mirror finish, followed by electrochemical etching to remove a mechanically damaged surface layer. It was mounted on a sample holder made of copper by mechanical anchoring, and a layer of high-conductivity thermal grease was applied to enhance the thermal contact. The sample holder was coupled via an indium foil onto the cold finger of a helium cryostat (displex). The sample temperature was controlled in the same way as the plutonium experiment, with the silicon diode sensor buried directly underneath the sample. The entire assembly was enclosed in a vacuum shroud made of beryllium. The refrigerator containing the sample assembly was mounted on a four-circle Kappa diffractometer. The incident x-ray beam is 8.0 keV in photon energy and has a cross section of 0.5 mm x 0.5 mm. Intensity of the incident beam was monitored by a He gas ion chamber. The scattered beam was defined by a pair of slits and detected by a scintillation detector.

After proper orientation of the Cu crystal by its Bragg peaks, TDS intensities were measured as selected wavevectors in reciprocal space. During the x-ray measurement, the sample temperature was slowly ramped between 10 K and 200 K to allow near thermal equilibrium at all times.

When temperature is changed, the lattice constant of Cu would shift slightly due to thermal expansion; meanwhile the sample’s height will also change because of the expansion of the displex cold finger. These effects were both carefully calibrated and

compensated for. By monitoring the sample temperature reading, diffractometer angles for each selected momentum transfer, as well as the sample's position, were constantly adjusted during the data acquisition. Meanwhile it was also helpful having a well-polished sample surface, which ensures constant incident and outgoing angles at each momentum transfer regardless of the sample's height, therefore minimizing the thermal drift of the signal.

6.3.2 Data and analysis

Figure 6.1(a) shows the measured x-ray intensity (circles) as a function of sample temperature at wavevector **q** = (1.1, 1.1, 1.1), in units of $2\pi/a$, where a is the lattice constant of Cu. At this momentum transfer only the longitudinal phonon mode would give a non-zero contribution to the scattering. The curves plotted in Fig. 6.1(a) are numerical simulations to the TDS temperature dependence, assuming a phonon frequency of 0.5, 1.5, 2.5, 3.5, and 4.5 THz, respectively. To better compare the overall shapes of these curves, each of them has been shifted and rescaled vertically so that the two end points match the

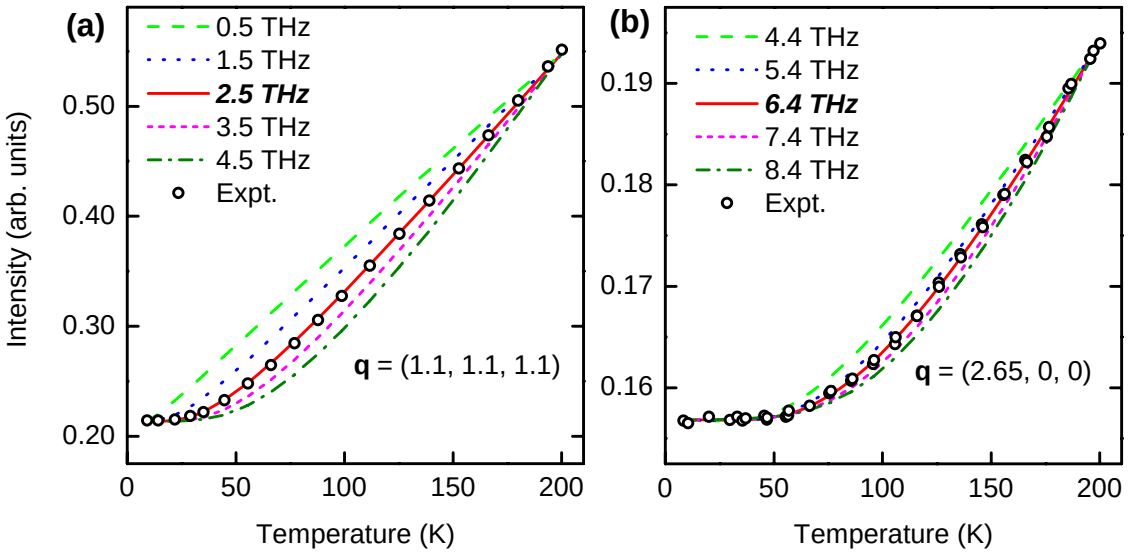

Figure 6.1. Simulated and experimental TDS intensities as a function of temperature for **q** at (a) (1.1, 1.1, 1.1) and (b) (2.65, 0, 0).

experimental data.

The shape of the temperature-dependence data curve begins with a horizontal segment at low temperatures, where the phonons are frozen out and the TDS intensity is dominated by zero-point vibrations. When temperature is raised, the intensity turns upward due to the increasing phonon population. The "threshold" for this upturning depends on the frequency of the phonon mode, which is the origin of the differences in curve shapes for the different assumed phonon frequencies. Such dependence therefore permits a unique determination of the phonon frequency.

The data analysis involves a straightforward procedure to solve for the phonon frequency based on the measured intensity curve. High-order TDS are accounted for with Debye-model approximation; while knowledge of the absolute intensity scale is not required. The analysis is also free from any arbitrary vertical shift to the intensity curve. The possible background intensities, including Compton scattering, defect and impurity scattering, ambient scattering, etc., will not affect our result as long as they are independent

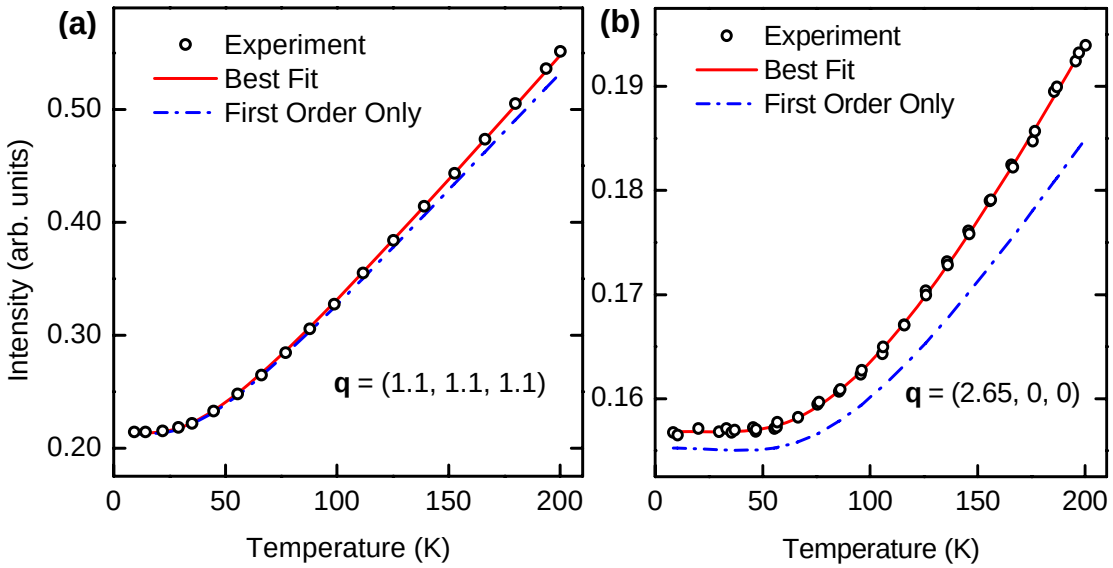

Figure 6.2. Comparison of total and first-order TDS intensities at (a) (1.1, 1.1, 1.1) and (b) (2.65, 0, 0).

of temperature. The analysis of the experimental data in Fig. 6.1(a) yielded the result of $\omega = 2.5$ THz, which agrees well with the available neutron scattering data [3].

Another set of data is presented in Fig. 6.1(b), with momentum transfer being **q** = (2.65, 0, 0). Again, only the longitudinal mode contributes. This mode has a higher frequency of 6.4 THz, and hence a relatively low TDS intensity; which is evidenced by the higher relative noise level in the data compared to Fig. 6.1(a). Nevertheless, the frequency of the mode can be readily extracted from the data, albeit with a larger uncertainty.

Figures 6.2(a) and 6.2(b) present the same two cases again, with the first-order contributions plotted in comparison with the total TDS intensity. If the first-order curves in Fig. 6.2(a) is appropriately shifted and rescaled in the vertical direction, it would overlap the solid curve almost exactly. As previously discussed, a first-order analysis suffices in this case. For the case in Fig. 6.2(b), high-order correction becomes significant, and a first-order-only analysis would give rise to an error of about 6%. In general, our way of estimating the high-order intensities with the Debye model worked well. In a further test, the derived phonon frequencies are almost the same when we replaced the Debye model with the known force constants of copper.

The cases presented in Fig. 6.1 involve just the longitudinal mode due to polarization selection. To probe their corresponding transverse modes, one should select a different polarization configuration at equivalent wavevectors in reciprocal space. For instance, the wavevector (1.1, 1.1, 1.1) is equivalent to wavevectors ($l \pm 0.1$, $m \pm 0.1$, $n \pm 0.1$) in reciprocal space, with *l*, *m*, *n* being arbitrary integers. When we set **q** = (1.9, 1.9, 0.1), a significant contribution from the two degenerate T[111] transverse modes would be present. In this case, although the longitudinal mode is not forbidden, the data analysis still involves only one unknown frequency, and the longitudinal contribution are simply calculated based on the frequency already deduced from the previous analysis at **q** = (1.1, 1.1, 1.1). For dispersion relations along the [011] direction, there exist two non-degenerate transverse modes, yet with proper polarization selections the two transverse frequencies

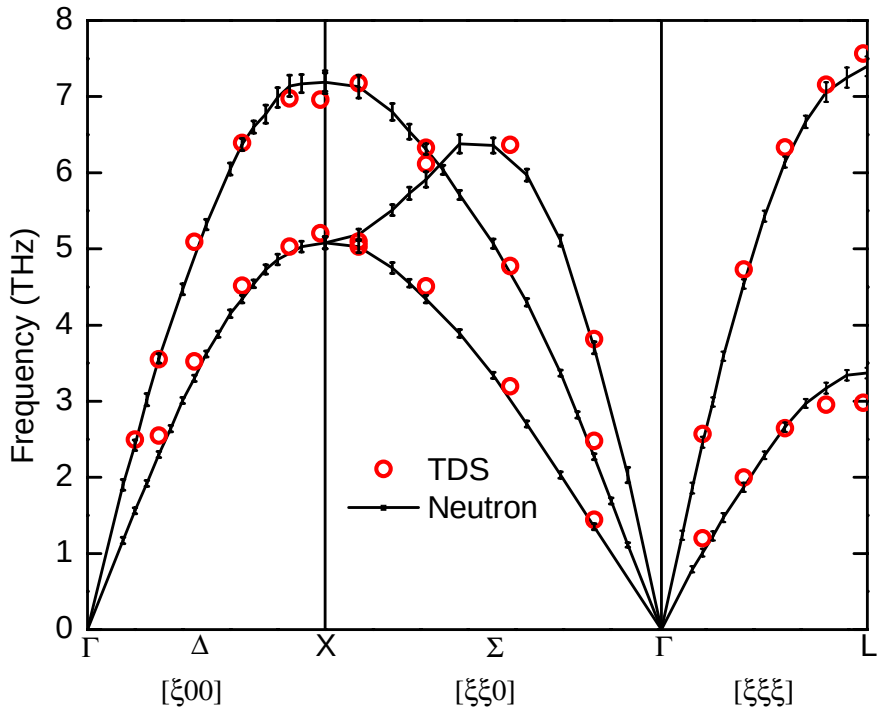

Figure 6.3. Phonon dispersion relation of Cu deduced from TDS temperature-dependence data (circles), in comparison with prior neutron scattering measurements.

can be independently determined once the longitudinal mode is solved. .

We made measurements for phonon modes along the three major high-symmetry directions: [001], [011], and [111] in Cu's reciprocal space. Figure 6.3 presents the full phonon dispersion curves of Cu extracted from the experiment. Results from our TDS analysis (circles) are in excellent agreement with prior neutron measurements taken at 296 K [3] (solid lines).

This work is therefore a successful demonstration of our new approach, which is essentially a calorimetric measurement carried out in reciprocal space based on TDS. Conceptually, the energy analysis in IXS is replaced by a thermal analysis in the present method: the heat content in the system at each point in momentum space is characterized by the phonon populations, which are measured by x-ray TDS intensities. The new

approach was hence given the name of momentum resolved x-ray calorimetry. Force-constant models are no longer a necessity for TDS studies, and the data analysis has also become simple and straightforward. This development therefore marks a further extension to the potential application of TDS as a probe of phonons.

List of References

[1] P. H. Dederichs and H. Schober, in *Metals: Phonon States, Electron States and Fermi Surfaces*, edited by K.-H. Hellwege and J. L. Olsen, Landolt-Börnstein, New Series, Group III, Vol. 13, pt.a (Springer-Verlag, Berlin, 1981), p. 96.

[2] M. Holt, P. Czoschke, H. Hong, P. Zschack, H. K. Birnbaum and T.-C. Chiang, *Phys. Rev. B* **66** (2002) 064303.

[3] E. C. Svensson, B. N. Brockhouse, and J. M. Rowe, *Phys. Rev.* **155** (1967) 3.

7 Summary and Outlook

Rich information are contained in x-ray thermal diffuse scattering (TDS) about the dynamics of crystal lattice, and our works have proved TDS a powerful tool for research related phonon dispersions. It is interesting to notice that TDS and phonon inelastic x-ray scattering (IXS) are essentially the same physical process, yet with different emphasis when referred to as experimental methods. IXS detects phonons by resolving the subtle energy shift in scattered photons; its measurements and interpretations are fairly straightforward. However, to achieve a stringent energy resolution of $\Delta\omega/\omega < 10^{-6}$, it has to sacrifice the intensity of the signal by several orders of magnitude compared to other typical x-ray techniques. TDS, in contrary, is a method that relies on accurate intensity measurements in the expense of energy resolution. The data collection is hence much simpler and faster, giving this method a unique advantage that may be desirable for many problems. Meanwhile the lack of energy resolution also poses a major drawback to this method. Determination of phonon frequencies is always indirect and could be sensitive to undesired backgrounds and noises. A careful design of the data modeling is also essential for successful analyses.

Further research aimed at improving the TDS method in its robustness and applicability has been proposed and is currently being carried out. One direction that seems promising is introducing intermediate energy or wavelength resolution into the measurement of TDS signals. In this way the x-ray Compton scattering could be utilized as an internal reference to TDS intensities for better determination of the phonon energies. In the future, it would also be ideal if TDS can be fully combined and integrated with the technique of IXS; since they represent the two ends of the same physics, complementary

use of the two methods should be much beneficiary to studies of lattice dynamics in various real systems.

In terms of application, perhaps the most suitable field for TDS is phase transitions. Once the basic phonon structure is known (from TDS or other methods), it is fairly straightforward to carry out an analysis of the TDS intensities in terms of changes in the phonon structure, which is generally a simpler problem than directly inverting TDS patterns to yield an entire set of phonon dispersion curves. The quick data acquisition rate is also desirable for repeated measurements at different conditions such as temperature, pressure, or external field.

A broad scope exists for many other potential applications of TDS as well. Time-resolved TDS measurements at the newly-developed fourth generation synchrotron source could bring insights to lattice dynamics in ultrafast timescales. Meanwhile, it is also possible to perform spatially resolved measurements with x-ray beams in sub-micrometer-size, which may enable us to investigate the interactions between lattice dynamics with phenomena like stress, impurities, boundaries, electric or heat transport, etc. Finally, instead of looking for phonons, one could also utilize TDS as an *in situ* probe of sample temperature during their experiment had an accurate reading is not permitted. With continued development of technologies in synchrotron radiation and x-ray detection, TDS is a promising tool to facilitate our ever-increasing understandings of the microscopic world.

Author's Biography

Ruqing Xu was born on September 20, 1978 in the city of Huaiyin, Jiangsu Province, People's Republic of China. He graduated with honor from the Physics Department, Tsinghua University in 1999, and later earned his Master's degree in Physics from Tsinghua University in 2002 in the field of theoretical atomic and molecular physics. He became an experimental condensed-matter physicist after enrolling at the University of Illinois at Urbana-Champaign where he is receiving his Ph.D. in 2010. He will join the X-ray Science Division at Argonne National Laboratory as an assistant physicist.

Publications

Ruqing Xu and Tai-Chang Chiang, "Studying structural phase transitions with x-ray thermal diffuse scattering", *Phase Transitions* 83 (2010) 99.

Ruqing Xu, Hawoong Hong, and Tai-Chang Chiang, "Probing phonons and phase transitions in solids with x-ray thermal diffuse scattering", in *Diffuse Scattering and the Fundamental Properties of Materials*, edited by R.I. Barabash, G.E. Ice and P.E.A. Turchi (Momentum Press, Highland Park, 2009) 161.

Hawoong Hong, **Ruqing Xu**, Ahmet Alatas, Martin Holt, and Tai-C. Chiang, "Central peak and narrow component in X-ray scattering measurements near the displacive phase transition in $SrTiO_3$", *Phys. Rev. B* 78 (2008) 104121.

Ruqing Xu, Hawoong Hong, Paul Zschack, and Tai-C. Chiang, "Direct mapping of phonon dispersion relations in copper with x-ray calorimetry", *Phys. Rev. Lett.* 101 (2008) 085504.

Ruqing Xu, Joe Wong, Paul Zschack, Hawoong Hong, and Tai-C. Chiang, "Soft phonons in δ-phase plutonium near the δ–α' transition", *Europhys. Lett.* 82 (2008) 26001.

J. Wong, M. Krisch, D.L. Farber, F. Occelli, **R. Xu**, T.-C. Chiang, D. Clatterbuck, A.J. Schwartz, M. Wall, and C. Boro, "Crystal dynamics of δ fcc Pu-Ga alloy by high-resolution inelastic x-ray scattering", *Phys. Rev. B* 72 (2005) 064115.

Ruqing Xu and Tai-Chang Chiang, "Determination of phonon dispersion relations by

X-ray thermal diffuse scattering", *Z. Kristallogr.* 220 (2005) 1009.

J. Wong, M. Wall, A.J. Schwartz, **R. Xu**, M. Holt, H. Hong, P. Zschack, and T.-C. Chiang, "Imaging phonons in a fcc Pu-Ga alloy by thermal diffuse x-ray scattering", *Appl. Phys. Lett.* 84 (2004) 3747.

J. Wong, M. Krisch, D.L. Farber, F. Occelli, A.J. Schwartz, T.-C. Chiang, M. Wall, C. Boro, and **R. Xu**, "Phonon dispersions of fcc δ-Pu-Ga by inelastic x-ray scattering", *Science* 301 (2003) 1078.

Wei-Hua Zhang, **Ru-Qing Xu**, and Jia-Ming Li, "Silane photoabsorption spectra near the Si 2p thresholds: the geometry of Si 2p excited SiH4**", *Chin. Phys.* 12 (2003) 275

Ru-Qing Xu, Wei-Hua Zhang, and Jia-Ming Li, "Determination of the geometric structure of core excited silane based on photoabsorption spectra near the Si 2p edges", *Chin. Phys. Lett.* 19 (2002) 1085

Ru-Qing Xu, Chang-Rong Su, Jun-Kai Xie, and Jia-Ming Li, "The potential surface in the ground electronic state of HCP with the isomerization process", *Sci. Chin.* A 45 (2002) 87